Hyperfine structure of the methanol molecule as traced by Class I methanol masers

Monthly Notices of the ROYAL ASTRONOMICAL SOCIETY

MNRAS **533,** 1714–1732 (2024) https://doi.org/10.1093/mnras/stae1815
Advance Access publication 2024 July 27

Hyperfine structure of the methanol molecule as traced by Class I methanol masers

I. I. Agafonova,[1] O. S. Bayandina ,[2] Y. Gong,[3,4] C. Henkel,[3,5]★ Kee-Tae Kim,[6,7] M. G. Kozlov,[8,9] B. Lankhaar,[10] S. A. Levshakov,[1]★ K. M. Menten,[3] W. Ubachs,[11] I. E. Val'tts[12] and W. Yang[3,13]

[1]*Ioffe Institute, 194021 St. Petersburg, 26 Polytekhnicheskaya str, Russia*
[2]*INAF–Osservatorio Astrofisico di Arcetri, Largo E. Fermi 5, I-50125 Firenze, Italy*
[3]*Max-Planck-Institut für Radioastronomie (MPIfR), Auf dem Hügel 69, D-53121 Bonn, Germany*
[4]*Purple Mountain Observatory, and Key Laboratory of Radio Astronomy, Chinese Academy of Sciences, 10 Yuanhua Road, Nanjing 210023, People's Republic of China*
[5]*Xinjiang Astronomical Observatory, Chinese Academy of Sciences, 830011 Urumqi, People's Republic of China*
[6]*Korea Astronomy and Space Science Institute, 776 Daedeokdae-ro, Yuseong-gu, Daejeon 34055, Republic of Korea*
[7]*University of Science and Technology, Korea (UST), 217 Gajeong-ro, Yuseong-gu, Daejeon 34113, Republic of Korea*
[8]*Department of Physics, Electrotechnical University 'LETI', 197376 St. Petersburg, Russia*
[9]*Petersburg Nuclear Physics Institute of NRC 'Kurchatov Institute', Gatchina, Leningrad District 188300, Russia*
[10]*Department of Space, Earth and Environment, Onsala Space Observatory, Chalmers University of Technology, Onsala 43992, Sweden*
[11]*Department of Physics and Astronomy, LaserLaB, Vrije Universiteit De Boelelaan 1081, NL-1081 HV Amsterdam, The Netherlands*
[12]*Astro Space Center, P.N. Lebedev Physical Institute of RAS, 84/32 Profsoyuznaya str, Moscow 117997, Russia*
[13]*School of Astronomy & Space Science, Nanjing University, 163 Xianlin avenue, Nanjing 210023, People's Republic of China*

Accepted 2024 July 11. Received 2024 June 28; in original form 2024 May 15

ABSTRACT

We present results on simultaneous observations of Class I methanol masers at 25, 36, and 44 GHz towards 22 Galactic targets carried out with the Effelsberg 100-m telescope. The study investigates relations between the hyperfine (HF) structure of the torsion–rotation transitions in CH_3OH and maser activity. By analysing the radial velocity shifts between different maser lines together with the patterns of the HF structure based on laboratory measurements and quantum-chemical calculations, we find that in any source only one specific HF transition forms the maser emission and that this transition changes from source to source. The physical conditions leading to this selective behaviour are still unclear. Using accurate laboratory rest frequencies for the 25 GHz transitions, we have refined the centre frequencies for the HF multiplets at 36, 44, and 95 GHz: $f_{36} = (36169.2488 \pm 0.0002_{\rm stat} \pm 0.0004_{\rm sys})$ MHz. $f_{44} = (44069.4176 \pm 0.0002_{\rm stat} \pm 0.0004_{\rm sys})$ MHz, and $f_{95} = (95169.4414 \pm 0.0003_{\rm stat} \pm 0.0004_{\rm sys})$ MHz. Comparison with previous observations of 44 GHz masers performed 6–10 yr ago with a Korean 21-m Korean Very Long Baseline Interferometry Network telescope towards the same targets confirms the kinematic stability of Class I maser line profiles during this time interval and reveals a systematic radial velocity shift of 0.013 ± 0.005 km s^{-1} between the two telescopes.

Key words: elementary particles – methods: numerical – techniques: spectroscopic – ISM: molecules – radio lines: ISM.

1 INTRODUCTION

Methanol (CH_3OH) masers,[1] widespread in the Milky Way and also found in nearby galaxies, have proven to be a powerful tool to study physical and chemical conditions in dense molecular clouds of different origins. There are two types of these masers, Class I and Class II (Batrla et al. 1987; Menten 1991). Class II masers are characterized by variable and complex emission line profiles, usually observed close to high-mass young stellar objects (Menten et al. 1992; Minier et al. 2001) and pumped by infrared (IR) radiation (Sobolev & Deguchi 1994; Cragg et al. 2005; Green et al. 2017).

In contrast, Class I masers arise frequently relatively far (∼ 1 pc) from radiating IR sources (Menten et al. 1986) and are associated with outflows and shock waves in the interstellar gas (Plambeck & Menten 1990; Cyganowski et al. 2009; Leurini et al. 2016; Ladeyschikov et al. 2020). The non-equilibrium inverted population of certain levels is created in this case by collisions with hydrogen molecules (Leurini et al. 2016). Amplification (exponential in non-saturated and linear in saturated maser regimes) of the stimulated emission requires high-velocity coherence which implies the absence of large velocity gradients along the beam path through the gas. The masering medium is thus stable and quiet. As a consequence, the observed maser lines are strong and have narrow and simple profiles, which allow us to determine the line position with high accuracy. This

★ E-mail: chenkel@mpifr-bonn.mpg.de (CH); lev.astro@mail.ioffe.ru (SL)
[1]Maser is short for Microwave Amplification by Stimulated Emission of Radiation.

makes Class I methanol masers a preferable tool for precise astronomical measurements, especially in cases where the analysis relies on the comparison of the radial velocities of different lines. In particular, this applies to the cases where astronomical observations are used to refine the data of laboratory spectroscopy: the observed lines are compared with reference line(s) whose rest frequencies are known with higher precision. Other examples are the estimation of magnetic fields by the Zeeman effect (Vlemmings 2008; Sarma & Momjian, 2009; Lankhaar et al. 2018; Momjian & Sarma 2019; Sarma & Momjian 2020) and the probing of the hypothetical variations of the electron-to-proton mass ratio, $\mu = m_e/m_p$ (Jansen et al. 2011; Levshakov et al. 2011; Daprà et al. 2017; Vorotyntseva et al. 2024).

Methanol is a non-rigid molecule with large-amplitude internal rotation of the methyl group around the CO bond (Hougen et al. 1994; Xu et al. 2008). There are two types of this molecule known: *A*-methanol with parallel proton spins of the hydrogen atoms in the CH_3 group, and *E*-methanol with a proton with antiparallel spin. Spin–rotation, spin–spin, and spin–torsion couplings lead to the formation of the hyperfine (HF) structure (Heuvel & Dymanus, 1973a; Heuvel & Dymanus, 1973b). For transitions commonly observed as Class I methanol masers (at 25, 36, 44, and 95 GHz) the hyperfine splitting between individual HF components is of order ~ 10 s kHz or, on the velocity scale, of hundreds to tens m s^{-1}. Thus, if problems under study require line position measurements with an accuracy of 10 m s^{-1} or better, effects of the HF structure should be taken into account.

To provide detailed information on the methanol HF structure, a set of high-precision laboratory measurements was carried out: in the range of $1 - 25$ GHz – with two molecular beam spectrometers (Coudert et al. 2015), and in the range $100 - 500$ GHz – also with two Lamb-dip spectrometers (Belov et al. 2016). These experiments made it possible to measure the centres of certain HF multiplets with very high accuracy (better than 1 kHz), but the HF structure itself was only partially resolved. Spectral resolution of Lamb-dip spectrometers – about 10 kHz, i.e. comparable to the HF splitting – is simply not high enough to resolve the HF structure. The molecular beam spectrometers have much better spectral resolution ($\lesssim 1$ kHz), but they work with supersonic beams, so that the individual HF components merge due to Doppler broadening. It is important to note that laboratory rest frequencies for 36, 44, and 95 GHz multiplets are measured with even lower accuracy (10–30 kHz) and the HF structure of these transitions has never been observed directly.

To evaluate the HF structure theoretically, Lankhaar et al. (2016) applied an original approach to define the effective Hamiltonian: they calculated a large part of couplings *ab initio* and estimated parameters for the remaining couplings by a fit to the laboratory spectra. The developed model was then used to calculate the Landé *g*-factors needed to convert the observed Zeeman splitting into the magnetic field strength. It was shown that in every torsion–rotation multiplet there are only a few 'favoured' HF components which can produce maser emission and it was assumed that only one of these components radiates from any source (Lankhaar et al. 2018).

Indeed, a single HF component has been detected in most of the OH masers thanks to the strong – units of MHz – HF splittings in the hydroxyl molecule (see e.g. reviews by Argon et al. 2000, or by Crutcher & Kemball 2019). For other masering molecules such as water (H_2O), ammonia (NH_3) or methanol with more compact HF splittings it remains so far unclear whether their maser emission includes a single component, or is a blend of several HF transitions.

Recently, the presence of a single HF component in methanol masers was confirmed by Levshakov et al. (2022, hereafter L22). Comparing the positions of the maser lines at 44 and 95 GHz in *A*-methanol they found that the velocity offsets ΔV between these lines cluster into two groups. Taking into account that both transitions have only two HF 'favoured' components, the revealed bimodality can be explained only under the assumption that in each source only one HF component is masering and these components are locked in the 44 and 95 GHz masers. This implies that if in the 44 GHz line an HF masering component is shifted to a higher frequency (blueward) relative to the multiplet centre, then in the 95 GHz line the masering component will also be shifted bluewards. The separation between the centres of both groups is $\Delta V = 0.022 \pm 0.003$ km s^{-1} which is very close to $\Delta V = 0.023$ km s^{-1} calculated by the quantum-chemical model of methanol in Lankhaar et al. (2016, 2018). This result implies that the cited model correctly predicts these favoured HF components, at least in the specified multiplets, and that Class I methanol masers can be used to explore the HF structure of the methanol molecule.

It was also found that the rest frequencies for the multiplet centres at 44 and 95 GHz are not known accurately enough. It is worth to note that the HF model itself does not involve the calculation of the torsion–rotation frequencies which are treated simply as external parameters. Corrections to the rest frequencies can be made either through new laboratory measurements or by comparison with lines whose rest frequencies are known with higher accuracy.

Another important conclusion relates to the formation mechanism of Class I masers. The 'favoured' components are almost identically pumped, but only one of them becomes a maser and this component changes from source to source. It is obvious that the process is modulated in some way by physical and chemical conditions in the masering medium. These conditions are still completely unknown and need to be clarified.

In this work, we continue to study Class I methanol masers, this time addressing the *E*-methanol molecule. With the Effelsberg 100-m radio telescope, we observed *E*-methanol masers at 25 and 36 GHz together with the *A*-methanol maser at 44 GHz towards 22 Galactic targets. One aim is to investigate the masering HF components in *E*-methanol and to determine whether they show the same properties as the masering components in *A*-methanol, i.e. the existence of only a few favoured HF transitions and the presence of only a single masering HF component in any source.

Another aim is to correct the poorly known rest frequencies for the 36, 44, and 95 GHz HF multiplets using as a reference accurate laboratory measurements of the 25 GHz transitions. The implications of these new frequencies for the existing limits on $\Delta\mu/\mu$ variations as well as possible mechanisms of Class I maser formation will be considered in forthcoming papers.

2 TARGET SELECTION AND OBSERVATIONS

To search for suitable Class I methanol maser sources, we used the Red *MSX* Source (RMS) catalogue[2] observed by Kim et al. (2018), and the Bolocam Galactic Plane Survey (BGPS) sources[3] observed by Yang et al. (2020). The surveys were performed at 44 and 95 GHz with the Korean Very Long Baseline Interferometry Network (KVN) in single-dish (21-m antenna) telescope mode. From these catalogues we selected targets with narrow emission lines located towards both the Galactic centre and anticentre and distributed across a wide range of Galactocentric distances, $5 \lesssim R \lesssim 13$ kpc.

[2]https://rms.leeds.ac.uk/cgi-bin/public/RMS_DATABASE.cgi
[3]https://irsa.opac.caltech.edu/data/BOLOCAM_GPS

Table 1. Summary of the observed sources, their Local Standard of Rest velocities, V_{LSR}, heliocentric, D, and Galactocentric, R distances. Given in parenthesis are masers' short names used therein and their other names cited in the literature.

No.	Source	R.A. (J2000) (h:m:s)	Dec. (J2000) (° : ′ : ″)	V_{LSR} (km s^{-1})	D (kpc)	R (kpc)	Ref.
1	Orion-KL (OKL)	05:35:14.17	−05:22:46.5	7.8	0.4	8.7	1, 2, 3
2	G208.816−19.239 (G208,OMC2)	05:35:27.14	−05:09:52.5	11.4	0.4	8.7	3, 4, 5
3	G173.719+2.698 (G173,S235)	05:40:53.30	+35:41:46.9	−17.0	1.7	10.0	5, 6
4	G183.348−0.577 (G183)	05:51:11.15	+25:46:16.4	10.0	2.0	10.3	7
5	BGPS7501 (B7501,S255)	06:12:52.90	+18:00:29.0	11.0	1.6	9.9	8, 9
6	RMS149 (R149,NGC2264,G203.316+2.055)	06:41:10.15	+09:29:33.6	7.2	0.6	8.9	3, 7
7	RMS153 (R153,G212.063−0.741)	06:47:13.36	+00:26:06.5	44.6	4.7	12.6	7
8	G013.097−0.146 (G013)	18:14:36.90	−17:38:47.5	43.7	3.8	4.7	10
9	BGPS2147 (B2147,G14.99−0.70)	18:20:22.00	−16:14:44.0	19.0	1.6	6.8	
10	G018.218−0.342 (G018)	18:25:21.99	−13:13:28.5	45.9	12.3	5.1	10
11	RMS2879 (R2879,G25.65+1.05)	18:34:20.89	−05:59:42.5	41.8	3.0	5.8	11
12	G029.277−0.131 (G029)	18:45:13.88	−03:18:43.9	60.1	3.6	5.5	10
13	BGPS4518 (B4518)	18:47:41.30	−02:00:21.0	91.6	5.2	5.0	10
14	RMS3659 (R3659,V645Cyg)	19:43:11.23	+23:44:03.6	22.5	2.2	7.5	8, 12
15	RMS3749 (R3749,V1318CygS)	20:20:30.60	+41:21:26.6	8.8	1.4	8.2	13
16	BGPS6815 (B6815,G81.302+1.052)	20:35:34.20	+42:20:13.0	13.7	1.3	8.2	10
17	BGPS6820 (B6820,G81.345+0.760)	20:36:58.10	+42:11:41.0	16.3	1.3	8.2	10
18	G102.650+15.786 (G102,L1157)	20:39:10.00	+68:01:42.0	0.8	0.25	8.4	14
19	BGPS6863 (B6863,G81.549+0.096)	20:40:28.70	+41:57:14.0	−6.5	3.5	8.6	10
20	RMS3865 (R3865,G82.583+0.201)	20:43:28.49	+42:50:01.8	10.3	1.4	8.3	10
21	G095.053+3.972 (G95)	21:15:55.63	+54:43:31.0	−85.6	9.0	12.8	7
22	G099.982+4.170 (G99,IC1396N)	21:40:42.40	+58:16:10.0	−0.9	0.75	8.5	15, 16

Note. References: 1. Barrett et al. (1971); 2. Haschick et al. (1990); 3. Liechti & Wilson (1996); 4. Menten et al. (1988); 5. Kang et al. (2016); 6. Gaia Collaboration (2018); 7. Kim et al. (2018); 8. Kim et al. (2019); 9. Breen et al. (2019); 10. Yang et al. (2020); 11. Bayandina et al. (2019); 12. Kalenskii et al. (1996); 13. Bae et al. (2011); 14. Kalenskii et al. (2010); 15. Kalenskii et al. (1992); 16. Fontani et al. (2010).

The observations with the Effelsberg 100-m radio telescope took place during the period 2022 January 26, 28–30 (project number 13-21). The position-switching mode was used with the backend eXtended bandwidth Fast Fourier Transform Spectrometer operating at 300 MHz bandwidth and providing 65 536 (2^{16}) channels for each polarization. The methanol lines were measured with the S14mm Double Beam RX (∼25 GHz) and the S7mm Double Beam RX (∼36 and 44 GHz) installed in the secondary focus yielding spectra at 25 GHz with an angular resolution of about 40 arcsec half-power beam width (HPBW) in two orthogonally oriented linear polarizations. The HPBWs were ≃ 30 and ≃ 25 arcsec at 36 and 44 GHz, respectively. The resulting channel separations are 0.055, 0.038, and 0.031 km s^{-1} at 25, 36, and 44 GHz, respectively. However, the true velocity resolution is 1.16 times coarser (Klein et al. 2012). The telescope pointing was checked every hour by continuum cross scans of nearby continuum sources, and the pointing accuracy was better than 5 arcsec. Depending on the object brightness and weather conditions, 4–24 scans, each lasting 2.4 min, were taken for every object. This yielded in the co-added spectra signal-to-noise ratio of several 10 s and up to several 100 s. Our sample of 22 objects is presented in Table 1. Column 2 lists maser source names as they are given in the corresponding catalogues along with their abbreviated names used therein and other names occurring in the literature (references in the last column).

Table 2. List of rest frequencies of the methanol transitions used in this work. The uncertainties are shown in parentheses.

Transition	f (MHz)	Ref.
$3_2 - 3_1 E$	24 928.701 05(10)	1
$4_2 - 4_1 E$	24 933.4702(3)	1
$5_2 - 5_1 E$	24 959.0789(4)	2
$6_2 - 6_1 E$	25 018.1234(4)	1
$7_2 - 7_1 E$	25 124.8719(4)	2
$4_{-1} - 3_0 E$	36 169.238(11)	3
$7_0 - 6_1 A^+$	44 069.430(10)	4
$8_0 - 7_1 A^+$	95 169.463(10)	5

Note. References: 1. Present paper; 2. Mehrotra et al. (1985); 3. Voronkov et al. (2014); 4. Pickett et al. (1998); 5. Müller et al. (2004).

3 LINE PROFILE ANALYSIS

3.1 Calculation procedure

The data reduction was performed using the GILDAS software's CLASS package.[4]The subsequent analysis of spectral data was performed in several steps. At the beginning, narrow spectral segments ($\sim$ 1.5 MHz) containing the methanol emission lines were extracted from the observed scans. For each interval, the baseline was determined and subtracted from the spectrum. Individual exposures were added up to enhance the signal-to-noise ratio, S/N. After that, the mean value of the rms uncertainties, $\sigma_{\rm rms}$, was calculated using spectral intervals not containing emission lines and/or noise spikes. The noise in the final spectra is often strongly correlated with a consequence that the apparent $\sigma_{\rm rms}$ comes out underestimated. Approximating the noise with the first-order autoregressive model, we corrected the noise amplitude as $\sigma^{\rm cor}_{\rm rms} = \sigma_{\rm rms}/\sqrt{(1-a_1^2)}$, where a_1 is the common Pearson correlation coefficient ($a_1 \simeq 0.7$ in our case). The obtained value of $\sigma^{\rm cor}_{\rm rms}$ was then assigned to the spectrum.

We note that absolute flux calibration was not performed due to the poor quality of calibration spectra at 36 and 44 GHz because of bad weather conditions at the time of observations. All following calculations are performed with line intensities given in units of main-beam brightness temperature, $T_{\rm mb}$. This does not in any way affect the results since for the aims of this work only the kinematic characteristics of the line profiles are relevant.

The transformation to the velocity scale occurred with the rest-frame frequencies listed in Table 2. The detailed description of our calculation procedure is given in Levshakov et al. (2019). Here, we repeat it only shortly.

Every line profile, which is a function of v on the velocity scale, $\phi(v)$, is fitted to a kinematic model, $y(v)$, represented by a sum of N Gaussian components. The line centre is defined as a point where the first order derivative of the profile function is equal to zero, $y'(v) = 0$. This point is further considered as the line radial velocity, $V_{\rm LSR}$. We note that in the present context the fitting model acts simply as a filter which is employed to smooth out eventual small-scale fluctuations which can hamper the evaluation of $y'(v)$.

The parameters of the fitting function are calculated by a standard χ^2 minimization:

$$\chi^2_\eta = \frac{1}{\eta}\sum_{i=1}^{n}\{[\phi(v_i) - y(v_i)]/\sigma^{\rm cor}_{\rm rms}\}^2, \quad (1)$$

where n is the number of channels covering the line profile, and η is the number of degrees of freedom, $\eta = n - 3N$.

The number of Gaussian components is chosen so that the χ^2_η function is minimized at the level of $\chi^2_\eta \simeq 1$ to avoid under or overfitting of the line profile. The uncertainty of $V_{\rm LSR}$, σ_v, is determined by three points $\{v_1, y_1; v_2, y_2; v_3, y_3\}$ with $v_1 < v_2 < v_3$ which include the flux density peak, $v_{\rm peak} \in (v_1, v_3)$:

$$\sigma_v = \frac{\sigma^{\rm cor}_{\rm rms}\Delta_{\rm ch}\mathcal{K}}{(y_1 - 2y_2 + y_3)^2}\,, \quad (2)$$

where $\mathcal{K} = \sqrt{(y_3 - y_2)^2 + (y_1 - y_3)^2 + (y_2 - y_1)^2}$, and the channel width $\Delta_{\rm ch} = v_2 - v_1 = v_3 - v_2$.

3.2 Reproducibility of radial velocities in Class I methanol masers at 44 GHz

A number of methanol maser transitions from this study have been previously observed using different facilities at different radio telescopes. We can compare the corresponding data in order to test the kinematic stability of Class I methanol masers over a 10-yr time lapse and to estimate possible systematics between telescopes.

Previously, such comparison was performed in L22 for the 44 GHz line in 10 objects observed with the KVN in single-dish mode in two surveys between epochs 2012 and 2016. In all objects, no significant shifts of the line centres were detected.

For objects from this study, Table 3 shows $V_{\rm LSR}$ evaluated for the 44 GHz lines taken in 2022 January with the Effelsberg 100-m telescope (HPBW $\simeq$ 40 arcsec) and the 44 GHz lines observed at different epochs with the KVN (HPBW $\simeq$ 65 arcsec). The spectral resolution was 0.031 and 0.053 km s^{-1} for the 100- and 21-m telescopes, respectively.

The last column in Table 3 gives the differences between the peak radial velocities, $\Delta V = V_{\rm Eff} - V_{\rm KVN}$. The weighted mean value of $\Delta V = 0.013 \pm 0.005$ km s^{-1} (1σ error of the mean) can be interpreted as a systematic error inherent to the performed observations. Different apertures, instrumental setups and observational conditions – all these factors contribute to the specified error. Taking into account the indicated complexity, we can consider the revealed systematic error as acceptable.

Another point is the physical stability of methanol masers themselves. As was already mentioned above, Class I methanol masers are suggested to be kinematically stable. In general, our results confirm this. Their fluxes – by definition a much more volatile characteristic than the velocity field – also vary very slowly on the time-scale of a few years which means that they emit to a large extent in a regime of saturation (Menten et al. 1988; Kurtz et al. 2004; Yang et al. 2020; Wenner et al. 2022). Assuming that these masers are confined to shocks and have characteristic sizes of $\sim$ 50 au, the time intervals when variability of the line position will be perceptible can be estimated as $\sim$ 15 yr (Leurini et al. 2016). Table 3 lists six objects observed within the 10-yr time lapse, and just three of them (R149, R153, R3865) from this set show statistically significant (over 5σ) velocity shifts from the mean value, whereas from 10 objects observed within 6 yr the comparable shift demonstrates only one (G029). Of course, statistics are rather poor and, additionally, without accurate absolute flux calibration we cannot conclude definitely whether these outliers are due to some shortcomings in the observations/data processing or due to real physical processes. This problem will be addressed in future studies.

[4]http://www.iram.fr/IRAMFR/GILDAS/

Table 3. LSR radial velocities of the $7_0 - 6_1 A^+$ transition at 44 GHz in Class I methanol masers measured with the KVN in single-dish (21-m antenna) mode ($V_{\rm KVN}$) and the Effelsberg 100-m telescope ($V_{\rm Eff}$) at different epochs. Statistical errors (1σ) in the last digits are given in parentheses.

Source ID	KVN Date	KVN $V_{\rm KVN}$ (km s^{-1})	Effelsberg Date	Effelsberg $V_{\rm Eff}$ (km s^{-1})	$\Delta V = V_{\rm Eff} - V_{\rm KVN}$ (km s^{-1})
R153	02.2012	44.644(6)	01.2022	44.684(2)	0.040(6)
R149	03.2012	7.216(7)	01.2022	7.251(2)	0.035(7)
R2879	05.2012	41.780(2)	01.2022	41.778(2)	−0.002(3)
R3659	10.2012	22.495(5)	01.2022	22.518(2)	0.023(5)
R3749	10.2012	8.826(4)	01.2022	8.840(4)	0.014(5)
R3865	10.2012	10.345(5)	01.2022	10.322(2)	−0.023(5)
B7501	11.2016	11.036(3)	01.2022	11.053(2)	0.017(4)
B2147	11.2016	19.033(17)	01.2022	19.048(2)	0.015(17)
B4518	11.2016	91.558(9)	01.2022	91.579(7)	0.021(11)
B6815(1)	11.2016	13.703(6)	01.2022	13.708(2)	0.005(6)
B6815(2)	11.2016	14.073(8)	01.2022	14.090(6)	0.017(10)
B6820(1)	11.2016	16.346(5)	01.2022	16.375(13)	0.029(14)
B6863	11.2016	−6.516(10)	01.2022	−6.488(5)	0.028(11)
G029	11.2016	60.100(5)	01.2022	60.141(2)	0.041(5)
G018(1)	11.2016	45.880(6)	01.2022	45.882(8)	0.002(10)
G018(2)	11.2016	46.498(13)	01.2022	46.500(18)	0.002(22)
				Weighted mean $\langle \Delta V \rangle$:	0.013(5)

3.3 Laboratory measurements of methanol HF rest frequencies at 25 GHz

High-dispersion laboratory spectroscopy of methanol torsion–rotation transitions at low frequencies were performed by J.-U. Grabow and S. A. Levshakov with the microwave molecular beam spectrometer at the Leibniz University Hannover in 2012. Among others, the following lines of the E-type ground torsional state ($v_{\rm t} = 0$) of CH_3OH were recorded: $J_2 \rightarrow J_1 = 3_2 - 3_1 E$ (24 928 MHz), $4_2 - 4_1 E$ (24 933 MHz), $5_2 - 5_1 E$ (24 959 MHz), and $6_2 - 6_1 E$ (25 018 MHz). The experimental setup was described briefly in Coudert et al. (2015). In the observed spectra, the HF structure was only partially resolved: we saw bi- and trimodal patterns where each mode consists of several blended lines. Primary processing of these spectra was aimed at calculating the accurate values of the HF multiplet centres which are now presented in table X in Coudert et al. (2015). The reconstruction of the methanol HF structure was out of the scope of that work. Recently, the observed morphology of the line shapes at 25 GHz was studied more closely by Vorotyntseva & Levshakov (2024).

Here, we reprocess the obtained laboratory spectra in 2012 in order to see whether we can reveal the detailed HF structure of methanol lines in question. The idea behind this is that the convolved components, even if not fully resolved, affect nevertheless the shape of the line envelope and – assuming a sufficiently high signal-to-noise ratio – can be more or less accurately deconvolved. The spectra have a spacing of $\Delta f = 1.2$ kHz ($\Delta v = 0.014$ km s^{-1}), thus making it possible to distinguish components detached by ~ 10 s of kHz.

The measurements were made in a supersonic molecular beam (CH_3OH/Ne mixture) injected parallel to the axis of the Fabry–Pérot resonator. The CH_3OH emission was generated by an external excitation impulse of the corresponding frequency. Ideally, a standing wave is formed in the resonator with nodes exactly on the axis; this produces an emission signal in the form of a doublet consisting of two symmetric parts Doppler-shifted relative to the central node (resonance frequency) which will be referred to as image I and image II hereinafter. However, in the case of non-resonant excitation of the molecular emission and/or non-tuned resonator the resulting spectral profiles can come out distorted (Grabow 2004, 2011). It is clear that parameters extracted from such profiles also can be biased.

Next, the Hannover University spectrometer was affected by residual magnetic fields of $B \lesssim 0.5$ Gauss – this may cause shifts in the component centres of about units of kHz. Special care is also required when measurements are carried out in the frequency range approaching the instrumental limit, which for the Hannover spectrometer is 26.5 GHz. In this case, the signal becomes weak and must be amplified, so that the general noise level increases even more due to the addition of the amplifier noise. It is obvious that the accuracy of the extracted parameters will be negatively impacted. Thus, both the raw data and the results of calculations should be treated with caution.

The experimental profiles of the 25 GHz lines are shown in Fig. 1 by dots with error bars representing the rms of the noise which was calculated using emission-free parts of the spectra on the left- and right-side to the emission line. The multiplet central frequencies listed in Table 2 were obtained by cross-correlating both images of the signal. Then these frequencies were used to transform the observed spectra to the velocity scale.

Below some comments are given on the spectra pictured in Fig. 1:

(i) Line $3_2 - 3_1 E$ – the second image of this line is slightly distorted and was discarded, only one image was used in our analysis. However, the S/N ratio is high enough (S/N = 90) to provide an accurate deconvolution of the subcomponents even from a single image.

(ii) Line $4_2 - 4_1 E$ – both images I and II are similar and were co-added to produce the resulting spectrum with S/N = 80. However, here the amplitude of one mode was noticeably lower than that of the other mode whereas in other lines both modes look more or less identical. This can hint at possible experimental flaws in the $4_2 - 4_1 E$ transition measurement. As a consequence, the derived parameters cannot be considered reliable despite small statistical errors, i.e. the revealed HF structure requires confirmations by further measurements/observations.

(iii) Line $5_2 - 5_1 E$ – both images were affected by a high noise. To reduce the noise, individual images were processed with moving average filters with a three-point window and then co-added.

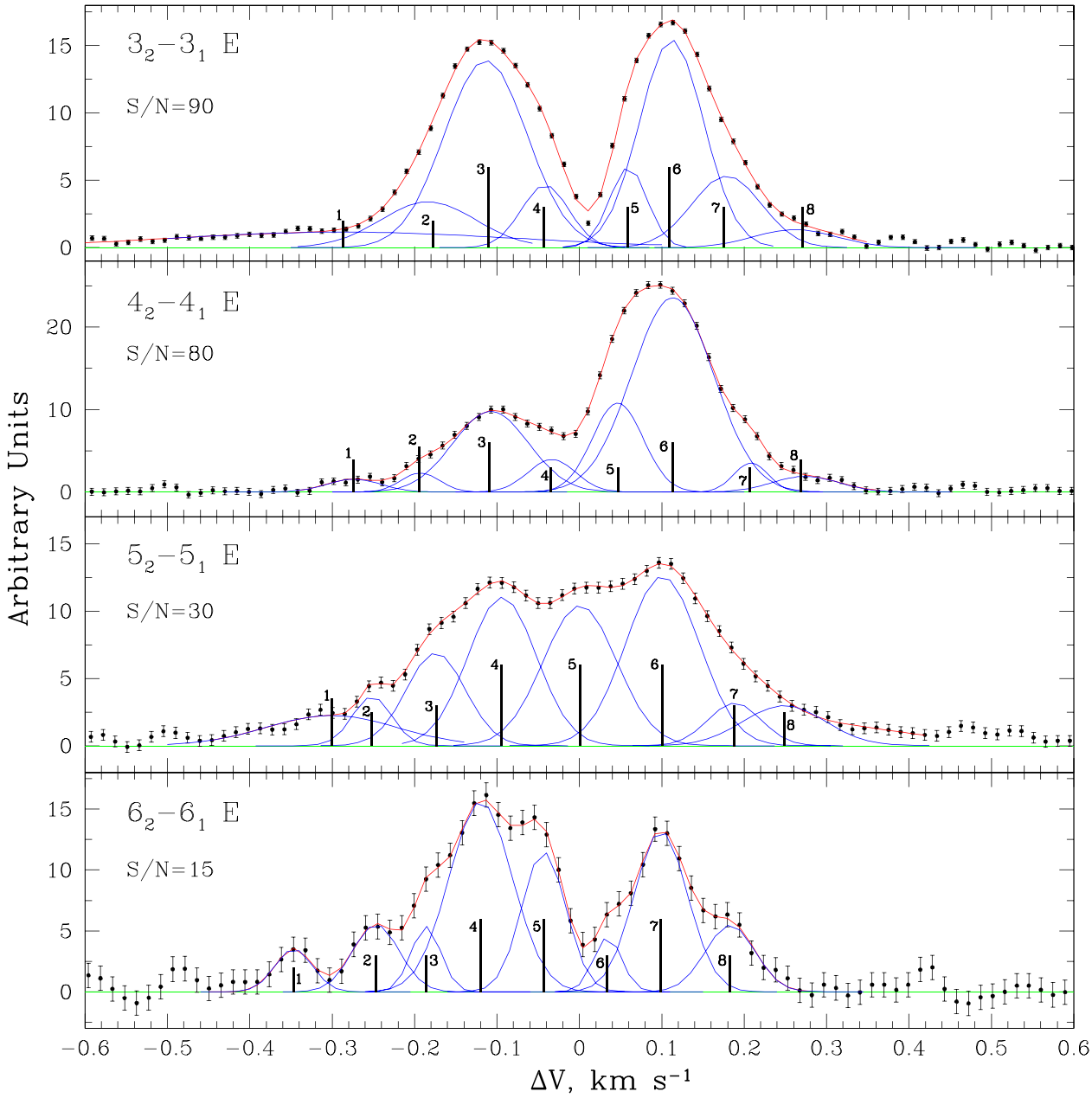

Figure 1. Dots with error bars display the laboratory spectra of methanol transitions at 25 GHz recorded with the molecular beam spectrometer of the Hannover University. The individual components are the blue curves, whereas their convolution is shown in red. The component fitting parameters are listed in Table 4.

(iv) Line $6_2 - 6_1 E$ – the images were filtered in the same way as for the $5_2 - 5_1 E$ line. Apart from general noise, one of the images revealed also an extended outlying fragment which could not be filtered out. This fragment was removed from the profile and the remaining parts were co-added with the second image.

The obtained line profiles were fitted to a model represented by a sum of N Gaussian components, each of which is characterized by three parameters – the component centre (f_i), the full width at half-maximum (FWHM$_i$), and the amplitude (A_i). The parameters were estimated by a standard χ^2 minimization. The value of N was chosen by iterations as the *minimum* number of components for which the condition $\chi^2_\eta \simeq 1$ is fulfilled.

The results of the calculations are presented in Table 4 with individual components pictured in Fig. 1 in blue. The parameter errors given in Table 4 are purely statistical (obtained by inversion of the Hesse matrix). However, due to the reasons mentioned above (line distortion, residual magnetic fields) there could also be systematic errors of similar values. We note that the Gaussian subcomponents have different FWHMs ranging from FWHM $\sim$ 0.05 to $\sim$ 0.5 km s^{-1}. Most likely, the narrowest components represent single HF lines, whereas components with larger dispersions are blends of close HF components which cannot be resolved with the current S/N and spacing in the data available.

Another result worth noting is the presence of a strong component near the multiplet centre in the $5_2 - 5_1 E$ and $6_2 - 6_1 E$

Table 4. Parameters of the HF components evaluated from the fitting of the methanol laboratory lines shown in Fig. 1. The line centre, full width at half-maximum, and amplitude are labelled as V_i, FWHM$_i$, and $\mathcal{A}_i$, respectively. The frequency offsets, $\Delta_i f$, are given relative to the central frequency f_0, also given in Table 1. Component numbers (1st column) correspond to those depicted in Fig. 1. Statistical errors (1σ) in the last digits, calculated via inversion of the Hesse matrix, are given in parentheses.

No.	V_i (km s^{-1})	FWHM$_i$ (km s^{-1})	$\mathcal{A}_i$	$\Delta_i f$ (MHz)	V_i (km s^{-1})	FWHM$_i$ (km s^{-1})	$\mathcal{A}_i$	$\Delta_i f$ (MHz)
	$J = 3$, $f_0 = 24\,928.701\,05(10)$ MHz				$J = 5$, $f_0 = 24\,959.0789(4)$ MHz			
1	−0.29(6)	0.49(12)	0.60(12)	0.024(5)	−0.30(4)	0.19(8)	0.44(15)	0.025(3)
2	−0.177(9)	0.108(17)	0.42(6)	0.0147(7)	−0.252(19)	0.03(3)	0.06(6)	0.0210(16)
3	−0.111(3)	0.111(5)	1.54(6)	0.0093(2)	−0.174(9)	0.092(17)	0.67(11)	0.0144(8)
4	−0.043(6)	0.069(11)	0.34(5)	0.0035(5)	−0.095(6)	0.094(11)	1.04(11)	0.0079(5)
5	0.059(4)	0.052(7)	0.33(4)	−0.0049(4)	0.001(6)	0.101(12)	1.07(11)	−0.0001(5)
6	0.109(2)	0.086(4)	1.34(5)	−0.0090(2)	0.101(6)	0.107(11)	1.29(12)	−0.0084(5)
7	0.175(5)	0.094(9)	0.62(5)	−0.0145(4)	0.19(2)	0.11(4)	0.41(12)	−0.0157(16)
8	0.27(3)	0.12(5)	0.17(6)	−0.023(2)	0.25(7)	0.30(12)	0.6(2)	−0.021(5)
	$J = 4$, $f_0 = 24\,933.4702(3)$ MHz				$J = 6$, $f_0 = 25\,018.1234(4)$ MHz			
1	−0.27(2)	0.08(4)	0.13(6)	0.0228(19)	−0.35(3)	0.05(5)	0.20(18)	0.029(2)
2	−0.194(13)	0.06(2)	0.14(5)	0.0161(11)	−0.25(2)	0.07(4)	0.4(2)	0.0206(17)
3	−0.109(4)	0.107(8)	1.10(7)	0.0091(4)	−0.186(17)	0.04(3)	0.24(16)	0.0155(15)
4	−0.034(8)	0.072(16)	0.32(6)	0.0028(7)	−0.120(8)	0.090(16)	1.5(2)	0.0100(7)
5	0.047(3)	0.072(6)	0.84(6)	−0.0039(3)	−0.043(10)	0.063(17)	0.77(19)	0.0036(8)
6	0.114(2)	0.117(3)	2.92(8)	−0.0094(2)	0.03(2)	0.04(3)	0.19(15)	−0.0029(16)
7	0.207(8)	0.046(15)	0.16(5)	−0.0172(7)	0.099(9)	0.076(17)	1.1(2)	−0.0082(8)
8	0.27(2)	0.11(4)	0.23(7)	−0.0223(17)	0.18(2)	0.07(4)	0.4(2)	−0.0153(18)

Table 5. Velocity splittings between the HF modes of the partially resolved laboratory profiles of methanol lines (Fig. 1). Listed are the mode centres V_1 and V_2, and their differences $\Delta V = V_2 - V_1$. The 1σ uncertainties in the last digits are given in parentheses.

Transition	V_1 (km s^{-1})	V_2 (km s^{-1})	ΔV (km s^{-1})
$3_2 - 3_1 E$	−0.116(3)	0.111(3)	0.227(4)
$4_2 - 4_1 E$	−0.103(5)	0.095(5)	0.198(7)
$5_2 - 5_1 E$	−0.097(7)	0.100(9)	0.197(11)
$6_2 - 6_1 E$	−0.117(16)	0.100(4)	0.217(16)

lines (component #5 in Table 4 and in Fig. 1). Such a component is not seen in the $3_2 - 3_1 E$ spectrum. As for the $4_2 - 4_1 E$ line, since its profile is presumably distorted, the conclusions about the presence of a strong central component require additional laboratory measurements and/or astronomical observations.

Given in Table 5 are the splittings between two convolved HF modes. It is a useful parameter which can be utilized to test the quantum-chemical models (Coudert et al. 2015; Belov et al. 2016; Lankhaar et al. 2016; Vorotyntseva & Levshakov 2024), or to conclude whether the double-peak profile is produced by a chance overlapping of two separate lines or indeed by convolved HF components of the same torsion–rotation transition. It is seen that in our case the splitting does not demonstrate a dependence on the rotational angular momentum J – unlike the result reported for high J in Belov et al. (2016). Further on, comparing line profiles calculated on base of Lankhaar's methanol model (figs 2 and 3 in Lankhaar et al. 2016) with our laboratory profiles and their deconvolution, we see that for the $3_2 - 3_1 E$, $4_2 - 4_1 E$, and $5_2 - 5_1 E$ transitions near 25 GHz this model yields an unsatisfactory result and should be refined. In contrast to this we recall here that for the 44 and 95 GHz 2016transitions in A-methanol the model was very successful.

3.4 Astronomical observation of the methanol HF structure at 25 GHz

Table 5 shows that the splitting between two convolved HF modes of the methanol lines at 25 GHz is ~ 0.2 km s^{-1}. Being observed with a sufficiently high-spectral resolution, these modes could be distinguished in the recorded astronomical spectra, but in practice the resolved HF modes are rare occasions due to the large Doppler broadening which causes line merging. For instance, among our data set of 22 objects we detected only one system, namely, RMS3865, with the resolved HF modes in several methanol transitions at 25 GHz. In Fig. 2, the observed profiles of the $4_2 - 4_1 E$, $5_2 - 5_1 E$, $6_2 - 6_1 E$, and $7_2 - 7_1 E$ thermal emission lines are shown in black, whereas the fitting curves are depicted in red. All lines are weak with correspondingly low S/N $\simeq 7 - 15$, so a unique deconvolution into individual subcomponents is impossible. The parameters that can be more or less accurately estimated from the profile fitting are solely the FWHM and the splitting ΔV between two composite HF modes centred at the radial velocities V_1 and V_2. The corresponding values are given in Table 6.

The measured splittings ΔV coincide with those obtained in laboratory (see Table 5), thus supporting our assumption that the 25 GHz spectra towards RMS3865 represent two modes of the composite HF transitions and are not two separate overlapping lines. The object RMS3865 exhibits also a strong maser emission at 36 and 44 GHz with the corresponding lines shifted by -0.4 and -0.2 km s^{-1} relative to the centre of the described 25 GHz lines. Moreover, the kinematic models for the 36 and 44 GHz profiles are different. Consequently, the emissions at 36 and 44 GHz which could correspond to the observed 25 GHz emission fall in the wings of those maser lines and cannot be extracted, but in any case they are very weak and probably thermal. This indicates that the source RMS3865 is in fact a superposition of several spots, each with different composition of masering and thermally excited species and, hence, with different physical conditions. We note that

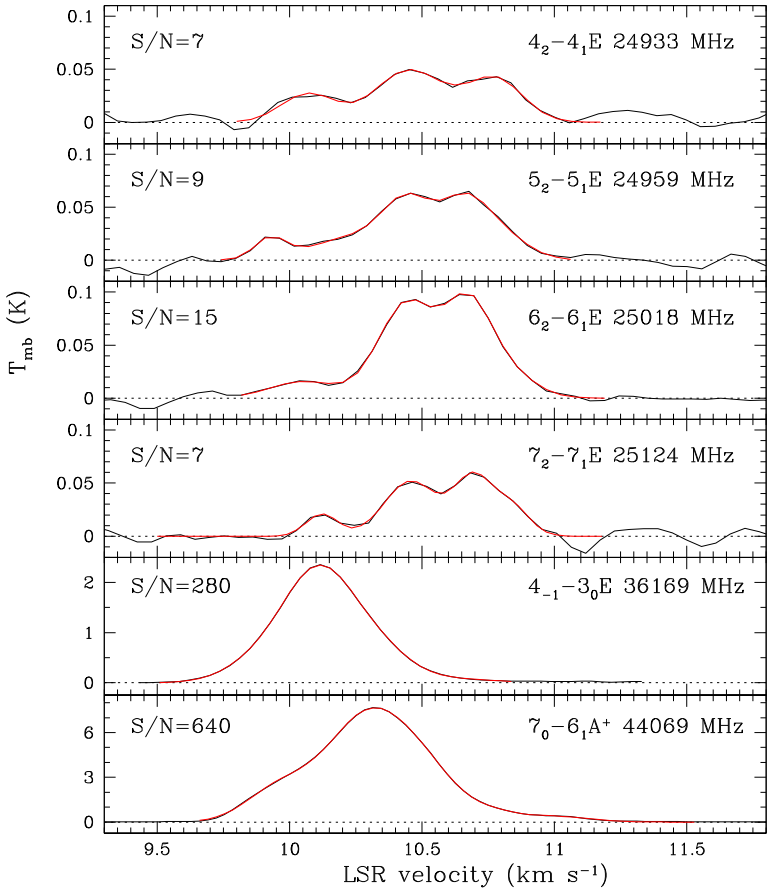

Figure 2. Thermal profiles of several methanol transitions at 25 GHz observed towards RMS3865. Strong maser lines at 36 and 44 GHz are shifted relative to the thermal 25 GHz lines by $\sim 0.5\,\mathrm{km\,s^{-1}}$. The observed lines are shown in black, and the fitting curves in red. The central double peaks in each panel represent a partially resolved HF structure of thermal lines (two main HF modes).

Table 6. Source RMS3865: fitting parameters for the thermal methanol emission lines at 25 GHz (Fig. 2). Listed are the HF mode centres V_1 and V_2, splitting between the modes $\Delta V = V_2 - V_1$, and the total line width FWHM. The 1σ uncertainties in the last digits are given in parentheses.

Transition	V_1 ($\mathrm{km\,s^{-1}}$)	V_2 ($\mathrm{km\,s^{-1}}$)	ΔV ($\mathrm{km\,s^{-1}}$)	FWHM ($\mathrm{km\,s^{-1}}$)
$4_2 - 4_1 E$	10.46(4)	10.76(10)	0.30(11)	0.5(8)
$5_2 - 5_1 E$	10.45(3)	10.66(3)	0.21(4)	0.5(5)
$6_2 - 6_1 E$	10.46(2)	10.66(2)	0.21(3)	0.5(3)
$7_2 - 7_1 E$	10.46(3)	10.69(3)	0.23(4)	0.5(5)

interferometric observations with high-spatial resolution show that such a picture is quite common (e.g. Voronkov et al. 2014).

As it was in the case of laboratory measurements, the observed astronomical profiles at 25 GHz towards RMS3865 show neither a decrease nor an increase in the HF mode splitting ΔV with changing J. Another fact to be mentioned is that the $4_2 - 4_1 E$ line profile itself and parameters evaluated from its fitting support our guess in the previous section that the recorded laboratory profile of the $4_2 - 4_1 E$ line is indeed distorted.

3.5 Sources with maser activity at 25 GHz

As stated above, the aim of this work is to reconstruct the HF structure of methanol transitions at 25, 36, and 44 GHz using sources with maser activity in all three families. The presence of emission lines near 25 GHz with detectable maser characteristics was the main selection criterion for the subsample considered in this section, since only for these lines we have accurate laboratory frequencies for individual HF components which can be used as a reference for further comparisons. As a maser characteristic we consider here primarily the narrowness of the line profiles. The preceding section shows that the thermally excited methanol lines near 25 GHz have FWHM $\gtrsim 0.5\,\mathrm{km\,s^{-1}}$. Thus, if we observe a line with FWHM $\sim 0.25\,\mathrm{km\,s^{-1}}$, it is most likely non-thermally excited, which could result in an inversion of the level populations.

In general, masers near 25 GHz are much less frequently observed as compared with those at 44 and 95 GHz (Ladeyschikov et al. 2019). As shown in Leurini et al. (2016), the inverted level populations of transitions near 25 GHz require much higher gas densities as compared to those at 36 and 44 GHz and this explains why a detection of maser activity in all three frequency bands is a relatively rare event. We confirm this statistics by our observations as well, when among 22 targets selected from the surveys at 44 and 95 GHz only nine show the required non-thermal emission near 25 GHz.

The emission line profiles for these nine sources are shown in Figs 3–5. The line peak velocities calculated as described in Section 3.1 are given in Table 7. Attribute R or L in the 2nd column of this table indicates which component of the HF multiplet at 44 GHz is masering: L stands for the strongest HF component blueward (on the velocity scale) from the torsion–rotation multiplet centre, and

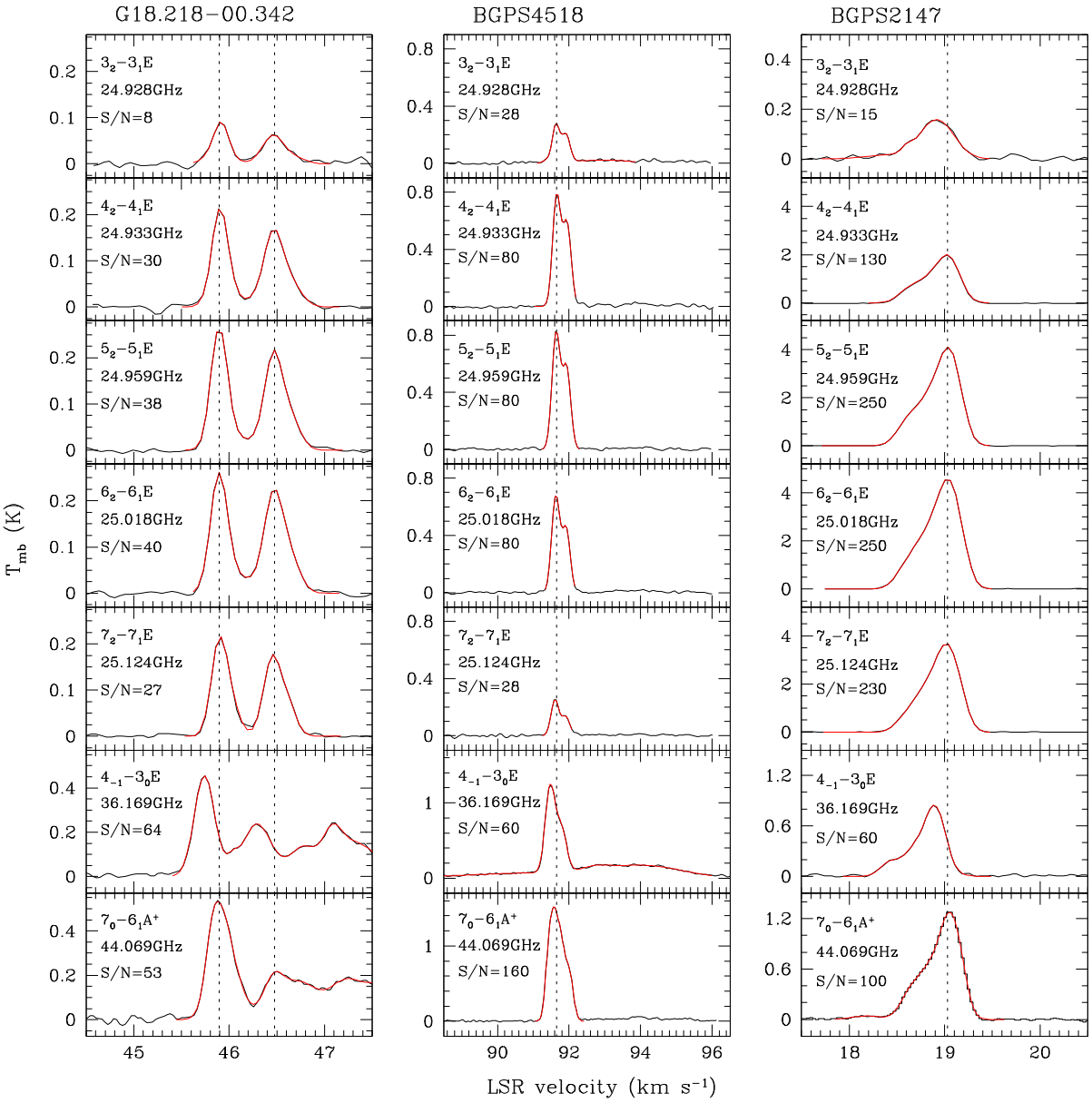

Figure 3. Black curves are the baseline subtracted emission lines of Class I CH_3OH masers of three families at 25, 36, and 44 GHz observed with the Effelsberg 100-m telescope towards the indicated maser sources. The fitting curves are shown in red. The methanol transition, its adopted rest frequency from Table 2, and the signal-to-noise ratio (S/N) per channel at the line peak are depicted in each panel. The vertical dotted lines mark the average position of the $5_2 - 5_1 E$ and $6_2 - 6_1 E$ lines used as the reference velocity for the 25 GHz transitions.

R, correspondingly, for the strongest 'red' HF component. These two groups, L and R, were defined in L22 by comparing the peak velocities of the 44 and 95 GHz maser lines (see table 6 and fig. 6 in L22).

Below brief comments are given on the selected nine sources:

(i) *G018.218−0.342*. All observed transitions near 25 GHz (Fig. 3) show double-peaked profiles with the peaks separated by $\sim 0.4\,\mathrm{km\,s^{-1}}$ which is twice the splitting between two convolved HF modes in thermally excited lines. The FWHM value for the first component, the same for all 25 GHz lines, is ~ 0.2, and $\sim 0.28\,\mathrm{km\,s^{-1}}$ for the second one. Thus, in G018.218−0.342, emission at 25 GHz comes from two maser spots clearly separated in the radial velocities and with masering activity involving only half of the HF multiplet structure.

The profiles of the 36 and 44 GHz lines are much more complex and include both the narrow maser and broad, possibly thermal components. Indefinite attributes L/R in the 2nd column of Table 7 are due to large errors in the peak velocities of the multimodal line at 95 GHz (see fig. 5 in L22) which makes it impossible to determine unambiguously which HF component, left or right, is masering.

(ii) *BGPS4518*. Again double-peaked maser line profiles are observed for all transitions near 25 GHz, with a weak broad, possibly thermal contribution to the $3_2 - 3_1 E$ line (Fig. 3). A strong asymmetric maser line is present at 36 GHz, also accompanied by broad emission. The maser line at 44 GHz shows a similar profile, but in this case without the broad component.

For all transitions: near 25 GHz, the lines have the same FWHMs of $0.55 \pm 0.02\,\mathrm{km\,s^{-1}}$ and the same apparent splitting between the

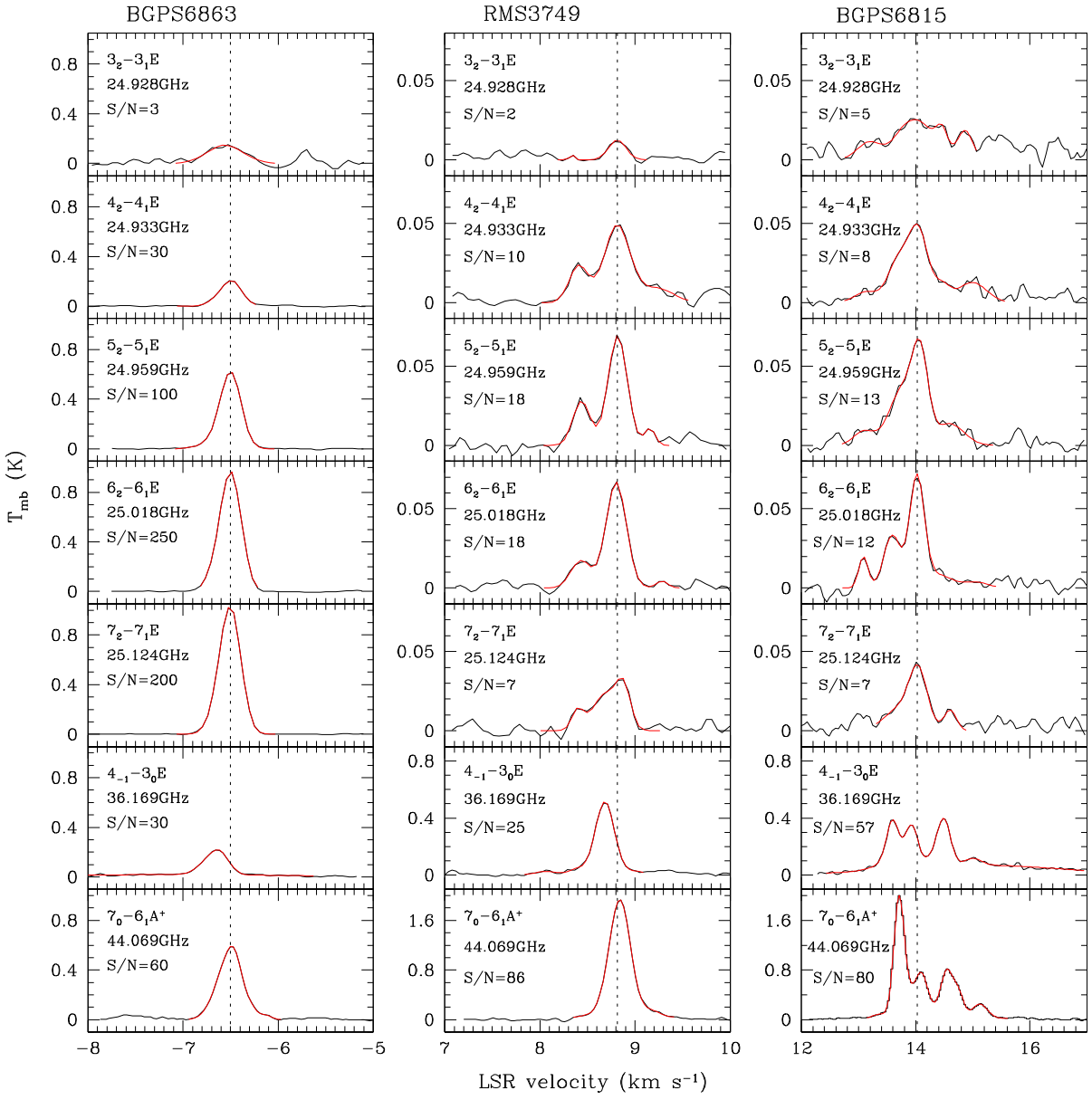

Figure 4. Same as Fig. 3.

components of 0.250 ± 0.010 km s^{-1}. This is close to the parameters measured for thermally excited lines with partly resolved HF structure (Section 3.3 and 3.4), so one might have thought that here both HF modes were masering. Yet it is not the case. All the line profiles at 25 GHz and the maser line at 36 GHz (with removed broad emission) can be perfectly fitted to the same two-component model, and the velocity difference between the components comes out to be equal for all species, i.e. the 36 GHz line as a whole is shifted in frequency relative to the lines at 25 GHz. However, the methanol HF structures at 25 and 36 GHz are different (it is more compact at 36 GHz – see Fig. 6 below), and if several HF components at 25 and 36 GHz were masering, then such uniform line transfer would not occur. Thus, in BGPS4518 we observe again two separate maser spots and in every spot merely half of the HF components (in fact only one – that with the largest Einstein A coefficient) is masering.

Unlike the 25 and 36 GHz lines, the maser at 44 GHz requires for the accurate line profile fitting a more complex (at least 4-component) model, so that a one-to-one correspondence between the model components at 44 GHz and those at 25 and 36 GHz cannot be established. That is why we give in Table 7 only one velocity value for this object, namely, that one which corresponds to the maximum amplitude of the line profiles.

The revealed discrepancy between the fitting models for the line profiles at 25 and 36 GHz on the one hand and for that at 44 GHz on the other demonstrates that in the present case the maser emission at 44 GHz does not exactly trace the maser emission at 25 and 36 GHz probably because of the presence of an additional maser spot radiating only at 44 and 95 GHz (see fig. 4 in L22). This emission may cause the velocity difference ΔV_{44-25} to be significantly biased.

(iii) *BGPS2147*. Among the 25 GHz transitions (Fig. 3), broad emission is observed in the $3_2 - 3_1E$ line with FWHM $= 0.46 \pm 0.04$ km s^{-1}, whereas other lines are masers with some broad contribution as well which leads to a relatively large value of FWHM $= 0.400 \pm 0.010$ km s^{-1}. At 36 and 44 GHz, the maser

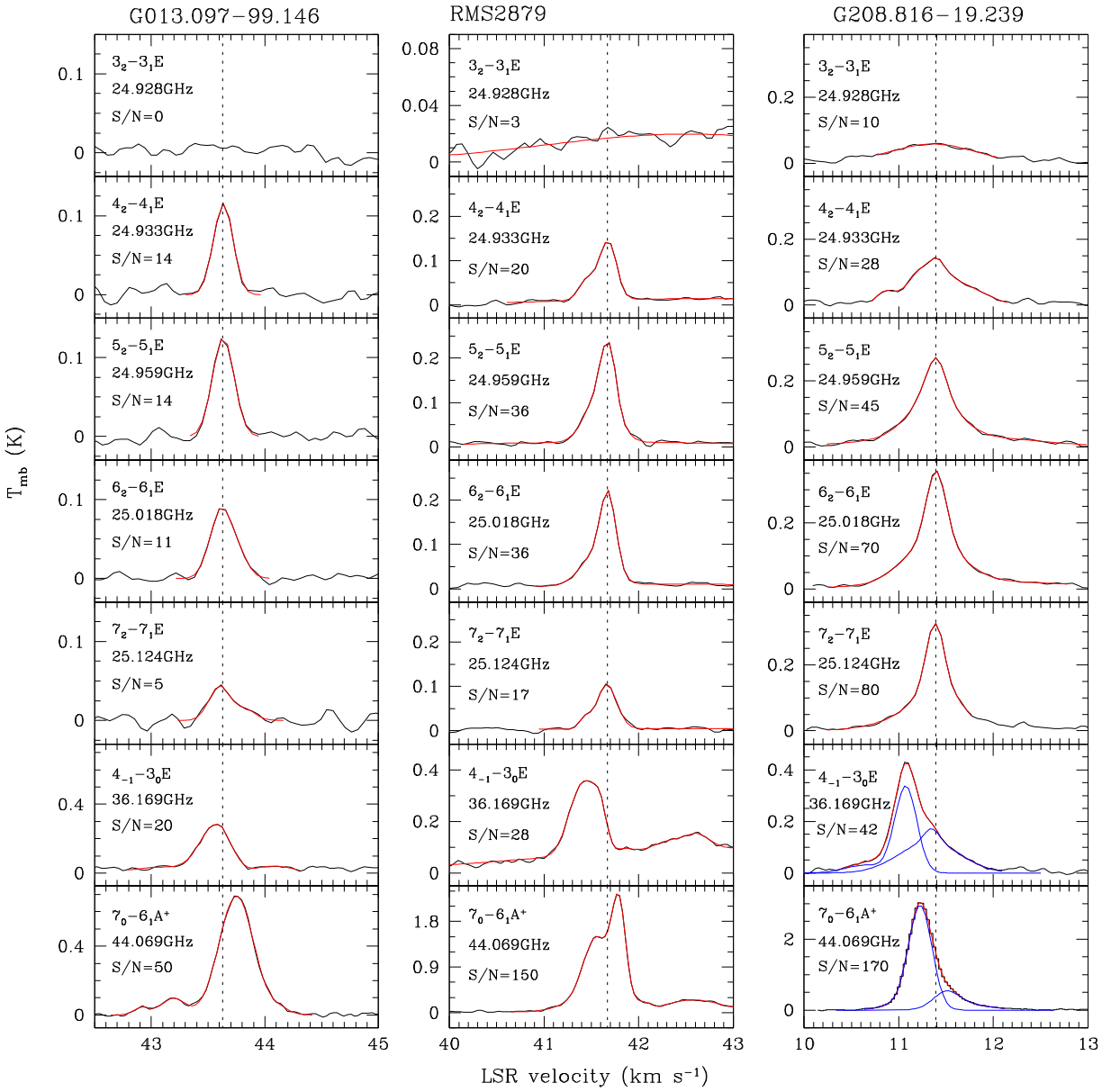

Figure 5. Same as Fig. 3. The blue curves in the panels $4_{-1} - 3_0 E$ and $7_0 - 6_1 A^+$ in the third column show two decomposed modes (see text).

emission, too, is accompanied by a weak broad component in the blue wings. All maser line profiles are simple and observed with high S/N $\gtrsim$ 100. This, in turn, results in the high accuracy of the calculated peak velocities which are determined with errors of only a few meters per second. In our data set, this object can be considered as a nearly perfect example of multiband maser emission.

(iv) *BGPS6863*. Here again the $3_2 - 3_1 E$ line is broad with FWHM $= 0.44 \pm 0.04\,\mathrm{km\,s^{-1}}$, whereas all other transitions at 25 GHz are masers with very narrow line profiles having FWHM $= 0.260 \pm 0.005\,\mathrm{km\,s^{-1}}$ (Fig. 4). The maser line at 36 GHz shows extended but weak emission in the blue wing, whereas the line profile at 44 GHz is dominated entirely by maser emission. This object is very similar to BGPS2147 and is a second fiducial example of the multiband maser emission in our sample.

(v) *RMS3749*. All of the present 25 GHz transitions are narrow with FWHM $= 0.25 \pm 0.05\,\mathrm{km\,s^{-1}}$, i.e. we observe definitely non-thermal emission, but it is weak (Fig. 4). The much stronger lines at 36 and 44 GHz, which are clearly masers, have the same line width. A weak contribution of a broad emission is also seen in the wings.

(vi) *BGPS6815*. At the position of the $3_2 - 3_1 E$ line at 25 GHz, there is an extended emission which is barely distinguishable from noise (Fig. 4). Other 25 GHz lines represent a blend of a few narrow (FWHM $\lesssim 0.3\,\mathrm{km\,s^{-1}}$) components which are resolved only in the strongest $6_2 - 6_1 E$ line. The components are separated by $\gtrsim 0.3\,\mathrm{km\,s^{-1}}$. The profiles at 36 and 44 GHz also exhibit complex multicomponent shapes.

In this work (L22), we have already analysed the 44 GHz line together with the line at 95 GHz, but considered only the velocities of the first (strongest) component – the measured difference $\Delta V_{44-95} = V_{44} - V_{95} = 0.030\,\mathrm{km\,s^{-1}}$ attributed this component as being the masering component right to the multiplet centre (fig. 6 in L22). However, the detected $6_2 - 6_1 E$ maser line at 25 GHz corresponds to the second maximum in the line profiles at 95, 44, and 36 GHz. Again, comparing the 44 and 95 GHz profiles (observed

Table 7. The line peak velocities, V_i, for a subsample of nine targets (10 maser spots) with maser activity detected in all three frequency bands at 25, 36, and 44 GHz. Listed in columns are: (1) shortened source names in accord with Table 1; (2) letters L or R indicate which component of the HF multiplet at 44 GHz is masering (see Fig. 6); L/R – indefinite attribution caused by a large error in the velocity difference $V_{44} - V_{95}$ (see text for details), no entry – object was not considered previously; (3)–(7) no entry – line cannot be extracted from the noise; (8) the reference velocity for the 25 GHz transitions, V_{25}, calculated as a weighted mean of the peak velocities of the $5_2 - 5_1E$ and $6_2 - 6_1E$ lines, or as a weighed mean of other 25 GHz transitions if the position of either $5_2 - 5_1E$ or $6_2 - 6_1E$ lines is an outlier (the second option is marked by an asterisk); (11) the difference between the peak velocity V_{36} at 36 GHz and the reference velocity at 25 GHz, $\Delta V_{36-25} = V_{36} - V_{25}$; (12) the difference between the peak velocity V_{44} at 44 GHz and the reference velocity at 25 GHz, $\Delta V_{44-25} = V_{44} - V_{25}$. The numbers in parenthesis are statistical errors (1σ) in the last digits.

Source	HF	$V_{3_2-3_1E}$ (km s^{-1})	$V_{4_2-4_1E}$ (km s^{-1})	$V_{5_2-5_1E}$ (km s^{-1})	$V_{6_2-6_1E}$ (km s^{-1})	$V_{7_2-7_1E}$ (km s^{-1})	V_{25} (km s^{-1})	V_{36} (km s^{-1})	V_{44} (km s^{-1})	ΔV_{36-25} (km s^{-1})	ΔV_{44-25} (km s^{-1})
(1)	(2)	(3)	(4)	(5)	(6)	(7)	(8)	(9)	(10)	(11)	(12)
G018(1)	L/R	45.911(15)	45.905(6)	45.896(5)	45.897(4)	45.906(8)	45.897(2)	45.741(6)	45. 882(8)	−0. 156(6)	−0. 015(9)
G018(2)	L/R	46.47(2)	46.474(10)	46.477(10)	46.477(10)	46.460(10)	46.477(7)	46.293(20)	46.500(18)	−0.184(20)	0.023(19)
B4518	L	91.653(7)	91.666(4)	91.652(4)	91.639(6)	91.616(10)	91.648(4)	91.487(6)	91.579(7)	−0.161(7)	−0.069(9)
B2147	R	18.92(2)	19.021(2)	19.034(2)	19.029(2)	19.015(2)	19.032(2)	18.890(4)	19.048(2)	−0.142(4)	0.016(3)
B6863	R	−6.56(3)	−6.494(6)	−6.502(2)	−6.500(2)	−6.505(2)	−6.501(2)	−6.642(10)	−6.488(5)	−0.141(10)	0.013(5)
R3749	R	8.815(30)	8.815(15)	8.818(11)	8.803(11)		8.817(5)*	8.684(8)	8.840(4)	−0.133(9)	0.023(6)
B6815	L	13.98(3)	14.010(35)	14.048(26)	14.023(11)	14.022(35)	14.023(11)*	13.928(10)	14.090(6)	−0.095(15)	0.067(9)
G013		43.633(8)	43.634(8)	43.626(14)	43.612(18)	43.632(7)	43.570(16)	43.749(10)	−0.062(18)	0.117(12)	
R2879	R	42.5(3)	41.671(14)	41.668(8)	41.670(5)	41.663(15)	41.669(3)	41.44(4)	41.778(2)	−0.23(4)	0.109(4)
G208		11.36(4)	11.390(13)	11.387(10)	11.393(5)	11.384(4)	11.392(4)	11.345(20)	11.515(18)	−0.047(20)	0.123(18)

with the KVN), we obtain for this second maximum a peak velocity difference of 0.008 ± 0.010 km s^{-1} and, hence, classify it as being a masering component to the left of the multiplet centre. Thus, in two neighbouring components of the 44 and 95 GHz lines we have two different HF transitions acting as masers what confirms our assumption that in BGPS6815 a superposition of separate maser spots is observed.

(vii) *G013.097−0.146*. The $3_2 - 3_1E$ line at 25 GHz is completely buried in noise (Fig. 5). Other 25 GHz transitions show weak maser emissions with FWHM $= 0.220 \pm 0.010$ km s^{-1}. A strong maser line at 36 GHz is accompanied by weak broad emission in both line wings. Some broad emission is also present in the blue wing of the maser line at 44 GHz.

(viii) *RMS2879*. A weak (S/N = 3) and very broad (FWHM $>$ 1 km s^{-1}) emission is tentatively detected at the position of the $3_2 - 3_1E$ line at 25 GHz (Fig. 5). This emission is also seen in the wings of relatively strong and narrow lines of other 25 GHz transitions which are definitely masers – their widths are FWHM $= 0.25 \pm 0.02$ km s^{-1}. The 36 GHz line is a combination of maser and broad, possibly thermal, emissions with a maser profile having FWHM $= 0.44 \pm 0.01$ km s^{-1} and showing an almost flat-topped profile. A comparison with the maser profile at 44 GHz reveals that the maser line at 36 GHz is in fact a blend of a few components. The difference $\Delta V_{36-25} = V_{36} - V_{25}$ between the peak velocities of the 36 and 25 GHz lines deviates greatly from all other ΔV_{36-25} values from Table 7, indicating that here we probably compare mismatched components. However, the flat top makes the unambiguous deconvolution impossible and, hence, the obtained ΔV_{36-25} value should be considered as an outlier. In turn, the double-peaked maser emission line at 44 GHz is perfectly fitted to a simple two-component model, so that the component centres can be determined with high accuracy. To note is that here the centre of the appropriate component just corresponds to the line peak velocity, thus making the difference ΔV_{44-25} even model-independent.

(ix) *G208.816−19.239*. This target resides in the Orion Molecular Cloud 2 and consists of several radiating spots overlapping in velocity space (e.g. van Terwisga et al. 2019). We note that such a picture is quite common for star-forming regions and molecular clouds (e.g. Pagani et al. 2017). The $3_2 - 3_1E$ line at 25 GHz is broad and probably thermal with FWHM $= 1.10 \pm 0.05$ km s^{-1} (Fig. 5). Other 25 GHz lines represent a combination of the broad with the narrow – maser – profiles with FWHM decreasing from 0.56 km s^{-1} for the $4_2 - 4_1E$ line to 0.30 km s^{-1} for the $7_2 - 7_1E$ line. In the profiles of the 36 and 44 GHz lines, a strong maser emission from other spot(s) is present, which manifests in large differences between the peak velocities of the transitions near 25 GHz and those at 36 and 44 GHz: ~ 0.3 and ~ 0.45 km s^{-1}, respectively. However, unlike RMS3865 (Section 3.4), the latter profiles show a pronounced asymmetry in the red wings and can be decomposed into two (multicomponent) modes using *the same* fitting model. This fact together with a high S/N makes it possible to calculate the centres of both modes with an accuracy sufficient to utilize the corresponding differences ΔV_{36-25} and ΔV_{44-25} in the subsequent analysis. The synthetic profiles of the two extracted modes are shown in blue in Fig. 5.

4 HF STRUCTURE OF CH_3OH AS RECOVERED FROM 25, 36, AND 44 GHZ MASER SPECTRA

4.1 'Favoured' HF components in the 25, 36, and 44 GHz torsion–rotation multiplets

The procedure described in this section is based on the assumption that in any one maser source only one HF component of the corresponding torsion–rotation multiplet is masering and this component can change from source to source. In order to determine which component is masering we employ the multiplet HF structure obtained either from laboratory measurements (for masers at 25 GHz) or from quantum-chemical calculations (for masers at 36 and 44 GHz) and consider the differences between the peak velocities of the observed 25, 36, and 44 GHz maser lines, $\Delta V_{36-25} = V_{36} - V_{25}$ and $\Delta V_{44-25} = V_{44} - V_{25}$. Since there are only a few (from 2 to 4) 'favoured' (i.e. which can act as masers; see below) HF transitions in every HF multiplet, the values ΔV_{36-25} and ΔV_{44-25} are expected to form separate groups which are then analysed to identify the HF components in action.

The velocity differences ΔV_{36-25} and ΔV_{44-25} are given in Col. 11 and Col. 12 of Table 7. For the reference velocity of the 25 GHz

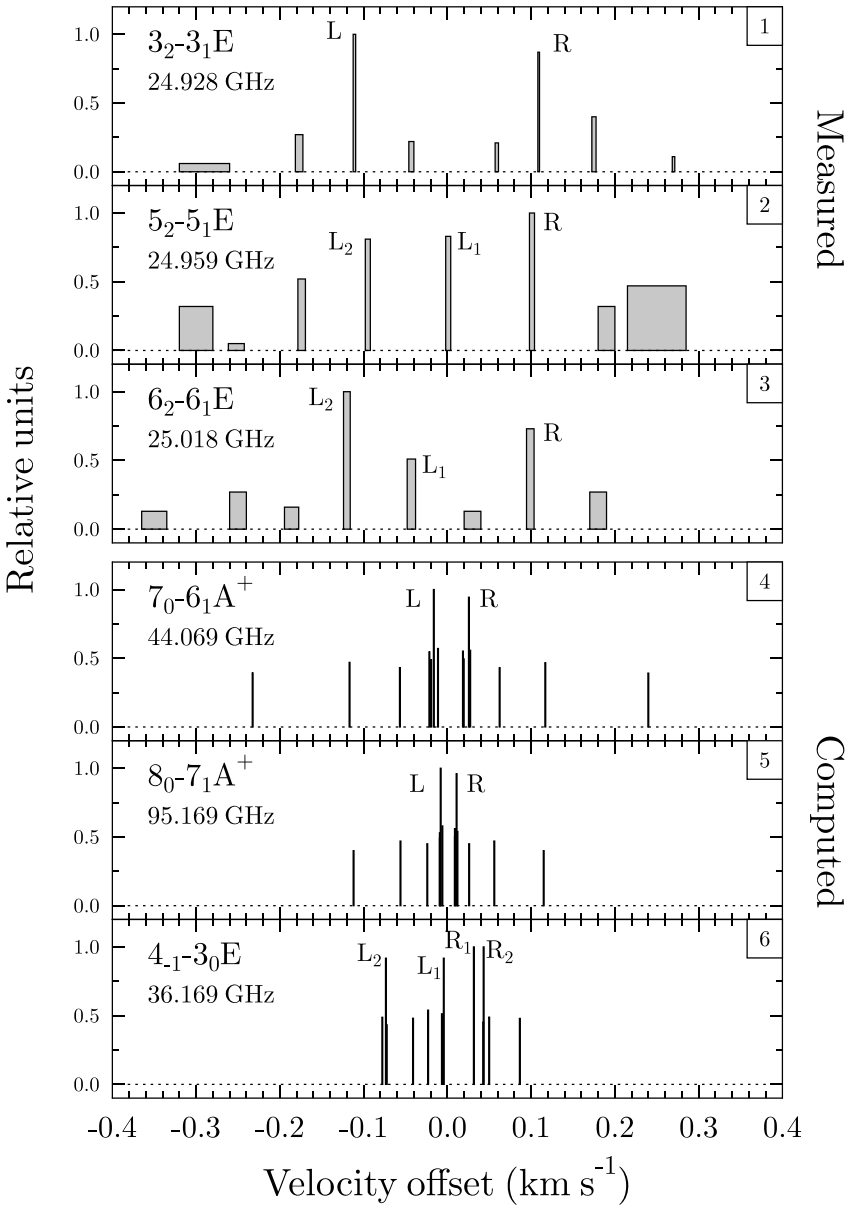

Figure 6. Templates of the HF structure of torsion–rotation multiplets used in this study. Individual HF components are represented by bars with bar's height proportional to the observed amplitude (the upper three panels) or to the Einstein A-coefficient (the lower three panels) of the corresponding transition. The velocity zero point is the multiplet centre. Indicated with letters are the 'favoured' HF components which potentially can form a maser. *Panels 1–3:* HF components deconvolved from the laboratory spectra (Fig. 1 and Table 4); the bar widths indicate the $\pm 1\sigma$ uncertainty interval of the line position. *Panels 4–6:* results of quantum-chemical calculations of the methanol HF structure (Lankhaar et al. 2016).

masers (Col. 8 of Table 7, V_{25}) the weighted mean of the peak velocities of the $5_2 - 5_1E$ and $6_2 - 6_1E$ lines is taken, since just these two lines are the strongest in our data set, thus allowing us to calculate the line centres with the highest possible accuracy. On the other hand, the measured mean velocity difference between the $5_2 - 5_1E$ and $6_2 - 6_1E$ lines of only 0.002 ± 0.002 km s^{-1} indicates that their positions coincide.

Fig. 6 schematically shows the HF components of different torsion–rotation transitions in methanol considered in this section. The zero velocity corresponds to the central frequency of the specified multiplet as given in Table 2.

The hyperfine component structure of the $3_2 - 3_1E$, $4_2 - 4_1E$, $5_2 - 5_1E$, and $6_2 - 6_1E$ transitions near 25 GHz was calculated from the laboratory spectral profiles (see Section 3.3). The individual HF components are plotted as bars at the velocity offsets ΔV given in Table 4 with bar's height scaling as the amplitude of the corresponding component, and bar's width – as the error in ΔV. The amplitude (emissivity), which is proportional to the Einstein A coefficient, determines the optical depth τ of the corresponding transition. Taking into account that maser emission exponentially depends on τ, it becomes clear why the HF components with the largest Einstein A coefficients are considered as 'favoured' for maser action.

As noted in Section 3.3, some bars in fact represent several convolved components; this is particularly true for the prominent bar to the right of the multiplet centre (indicated with R in Fig. 6) which

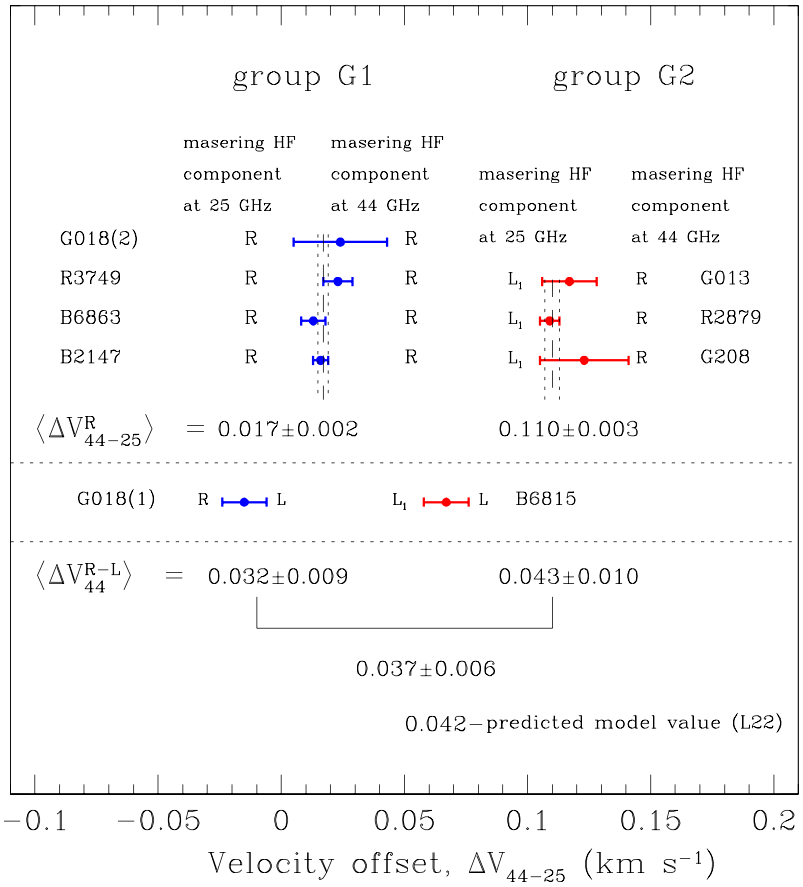

Figure 7. The difference $\Delta V_{44-25} = V_{44} - V_{25}$ between the peak velocities of maser lines at 25 and 44 GHz. The masering HF components labeled by L_1 and R at 25 GHz and L and R at 44 GHz are as indicated in panels 2, 3, and 4 in Fig. 6. See text for details.

is probably a close doublet with the splitting between components less than 0.010 km s^{-1}. On the other hand, strong components to the left of the centre form a broad doublet (best seen in the $5_2 - 5_1E$ transition with components indicated as L_1 and L_2) with a splitting of ~ 0.1 km s^{-1} and with one component very close to the multiplet centre.

The available laboratory measurements for the torsion–rotation transitions $7_0 - 6_1A^+$ at 44 GHz and $8_0 - 7_1A^+$ at 95 GHz are not fine enough to resolve the HF components (Tsunekawa et al. 1995; Müller et al. 2004), that is why we use here the HF structures computed by the quantum-chemical model of Lankhaar et al. (2016, 2018). Plotted by bars are only the strongest HF components, i.e. those with large Einstein A coefficients, with bar's height proportional to the corresponding coefficient. In general, computed structures are strongly model-dependent and require in every case experimental verification. As already noted in Section 1, by analysing previous observations of the 44 and 95 GHz masers in *A*-methanol (L22), we found that computed velocity offsets, ΔV, for the strongest (i.e. masering) HF components to the right (R) and to the left (L) of the multiplet centres correctly reproduce the observational data, i.e. for these transitions the model of Lankhaar et al. is adequate and can be utilized as a template. At 44 GHz, the computed offsets (on the velocity scale) are $\Delta V_{\rm R} = 0.026$ km s^{-1} and $\Delta V_{\rm L} = -0.016$ km s^{-1}, thus giving the splitting between the R and L components $\Delta V^{\rm R-L}_{44} = 0.042$ km s^{-1}. However, it is to emphasize once again that offsets (in frequencies or velocities) are calculated *relative* to the multiplet centre which is simply an external model parameter. In order to obtain the absolute (i.e. zero-point independent) frequencies of individual HF components an accurate value of the central rest frequency is needed.

The HF structure of the $4_{-1} - 3_0E$ torsion–rotation multiplet at 36 GHz (panel 6 in Fig. 6) was also computed by the quantum-chemical model mentioned above. At the moment we have neither laboratory nor astronomical data which can be used to verify the calculations. We note only that the computed structure looks very similar to that reconstructed from the laboratory spectra of the *E*-methanol transitions at 25 GHz with four potentially 'favoured'(strong) components: two close components (not resolved explicitly at 25 GHz) to the right of the multiplet centre (indicated as R_1 and R_2 in panel 6 of Fig. 6) and two distant components to the left (L_1 and L_2 in panel 6 of Fig. 6). This structure differs significantly from the HF structure at 44 and 95 GHz in *A*-methanol where only two favoured components – one to the right and one to the left of the centre – are present (and confirmed by astronomical observations).

The measured velocity differences, $\Delta V_{44-25} = V_{44} - V_{25}$, are plotted as points with error bars in Fig. 7. It is seen that the ΔV_{44-25} points with label R at 44 GHz, i.e. those with maser emission due to the *same* right-handed HF component, form, nevertheless, *two* compact and clearly distinguishable groups (referred to as G1 and G2): the G1 group with a weighted mean $\langle \Delta V^{\rm R}_{44-25} \rangle_{\rm G1} = 0.017 \pm 0.002$ km s^{-1}, and the G2 group with $\langle \Delta V^{\rm R}_{44-25} \rangle_{\rm G2} = 0.110 \pm 0.003$ km s^{-1}. These mean values together with their $\pm 1\sigma$ boundaries are indicated in

Fig. 7 with, respectively, dashed and dotted lines. The targets G013 and G208, shown in this figure, were not included in our previous data set and, accordingly, it was not known in advance whether they should have been marked with letters R or L. However, due to the closeness of their ΔV_{44-25} values to that of R2879 from the G2 group, we attribute G013 and G208 to the group G2 as well (i.e. the masering component at 44 GHz is R).

These two groups, G1 and G2, imply that 25 GHz masers are also formed by the emission at *two* different frequencies within the 25 GHz multiplets. The offsets of these frequencies relative to the multiplet centre can be assessed as follows. The separation between groups is

$$\langle \Delta V^{\rm R}_{44-25}\rangle_{\rm G2} - \langle \Delta V^{\rm R}_{44-25}\rangle_{\rm G1} = 0.093 \pm 0.004 \ \ {\rm km\ s^{-1}}\,, \qquad (3)$$

and, taking into account that the observed maser emission at 44 GHz is due to the same R-component of the HF multiplet, this value should correspond to the velocity splitting between two HF components of the 25 GHz transition. Looking at panels 3 and 4 of Fig. 6 where the HF structure of these multiplets is plotted one finds that the measured splitting of $\sim 0.093\,{\rm km\,s^{-1}}$ can be explained if we assume that the emerging groups are formed either (*i*) by the L_2 and L_1 components (splitting $0.096 \pm 0.008\,{\rm km\,s^{-1}}$) or (*ii*) by the R and L_1 components of the multiplets (splitting $0.100 \pm 0.008\,{\rm km\,s^{-1}}$). Note that the splitting between the extreme components L_2 and R is approximately $0.2\,{\rm km\,s^{-1}}$, i.e. twice the value obtained in equation (3). However, in the G1 group (Fig. 7) we have two targets, B2147 (Fig. 3) and B6863 (Fig. 4), both with broad and weak $3_2 - 3_1E$ lines and strong narrow maser lines in the other 25 GHz transitions. For these targets, the velocity difference between the centres of the maser and broad lines is 0.05 ± 0.03 and $0.10 \pm 0.03\,{\rm km\,s^{-1}}$, respectively, i.e. the maser emission is formed definitely redward to the centre of the broad profile. This means that the second option is realized, namely, that in the G1 group the masering component of the 25 GHz maser is R and in the G2 group – L_1 (see diagram in Fig. 7).

We would like to also emphasize that in these L_1 masers just a single L_1 component radiates and not components L_2 and R together as one might think. These components are almost equally detached from the multiplet centre (Fig. 6) and could therefore form a line centred at L_1. However, this line would have an FWHM $\gtrsim 0.5\,{\rm km\,s^{-1}}$ (see Table 6), whereas in the L_1 masers the observed lines are very narrow, FWHM $\sim 0.2 - 0.3\,{\rm km\,s^{-1}}$, which can be realized only for a single masering component.

In our data set, there are only three targets, G018(1), B4518, and B6815, with the left-handed (L) masering component at 44 GHz (Table 7), and we have to determine which of the possible HF components are masering at 25 GHz.

The values ΔV_{44-25} for these sources are $-0.015 \pm 0.009\,{\rm km\,s^{-1}}$ (G018(1)), $-0.069 \pm 0.009\,{\rm km\,s^{-1}}$ (B4518), and $0.067 \pm 0.009\,{\rm km\,s^{-1}}$ (B6815). According to the quantum-chemical model by Lankhaar et al. (2016, 2018), the velocity splitting between the 'favoured' HF components at 44 GHz should be $\Delta V^{\rm R-L}_{44} = 0.042\,{\rm km\,s^{-1}}$ (Fig. 6). Comparing these values with ΔV_{44-25} for the groups G1 and G2, it is evident that in G018(1) the masering component at 25 GHz is R and in B6815 is L_1. As for B4518, the masering component at 25 GHz is also R, but the value of ΔV_{44-25} is highly distorted due to some intervening emission at 44 GHz as it was already suggested in the description of this source in Section 3.5. Consequently, we exclude $\Delta V_{44-25} = -0.069\,{\rm km\,s^{-1}}$ from further considerations. Then, the velocity splitting between the R and L hyperfine components in the 44 GHz multiplet is $\Delta V^{\rm R-L}_{44} = 0.032 \pm 0.009\,{\rm km\,s^{-1}}$ and $\Delta V^{\rm R-L}_{44} = 0.043 \pm 0.010\,{\rm km\,s^{-1}}$ for the groups G1 and G2, respectively, yielding the combined weighted mean $\langle \Delta V^{\rm R-L}_{44}\rangle = 0.037 \pm 0.006\,{\rm km\,s^{-1}}$. This estimate is quite close (the difference lies within the $\pm 1\sigma$ uncertainty interval) to the predicted value of $0.042\,{\rm km\,s^{-1}}$ which can be considered as a good coincidence, especially taking into account that for each group only one target with the left-handed masering component at 44 GHz is available.

Now consider the velocity difference between the 36 and 25 GHz lines, ΔV_{36-25}. From the above analysis of ΔV_{44-25} we know for each of our targets which HF component is masering at 25 GHz, so that the difference ΔV_{36-25} can be led to a common reference point. With the L_1 component in the 25 GHz multiplet (coinciding with the centre of the multiplet, see panel 2 in Fig. 6) taken as such a reference, the recalculated values ΔV_{36-25} are plotted as points with error bars in Fig. 8. This time three separate groups are formed, each characterized by the values (weighted means) of -0.094 ± 0.007, -0.065 ± 0.004, and $-0.047 \pm 0.003\,{\rm km\,s^{-1}}$. These values are given relative to the *same reference*, indicating that every group in fact corresponds to a certain masering component at 36 GHz with differences between the groups indicating the separations between components. The splitting between the first and second components is then $0.029 \pm 0.008\,{\rm km\,s^{-1}}$ and between the second and third is $0.018 \pm 0.005\,{\rm km\,s^{-1}}$ (Fig. 8). Comparing these estimations with the computed HF structure at 36 GHz (panel 6 in Fig. 6) we easily identify the first group with the component L_1, the second – with R_1 (the predicted splitting R_1–L_1 is $0.036\,{\rm km\,s^{-1}}$), and the third – with R_2 (the predicted splitting R_2–R_1 is $0.012\,{\rm km\,s^{-1}}$). Note that the computed splitting between the components R_2 and R_1 of $0.012\,{\rm km\,s^{-1}}$ is underpredicted – such small difference simply would not be detected with our resolution and measurement errors – but in general we can conclude that the quantum-chemical model by Lankhaar et al. (2016, 2018) quite correctly reproduces the structure of the 'favoured' HF components in the $4_{-1} - 3_0E$ torsion–rotation multiplet at 36 GHz of *E*-methanol.

4.2 Comments on the recovered HF components in the 25, 36, and 44 GHz multiplets

As already noted above, our basic assumption is that each specific multiplet has only a few 'favoured' HF components which can participate in maser action and only one of them acts in any given source. Using only kinematic characteristics of the maser line profiles (namely, peak velocities) and employing templates of the multiplet's HF structure we determined which particular HF component is acting in every case. Here, we comment on possible physical mechanisms behind the revealed effects.

Hyperfine splitting structure in *E*-methanol at 25 GHz was recorded in laboratory experiments and then confirmed by observations of the thermally excited emission lines towards RMS3865. According to this structure, components with almost equally strong Einstein A coefficients are L_2, L_1, and R (panel 3 in Fig. 6). In our data set of 10 masers (nine targets), we detected six cases where the R component was masering, four cases with the L_1 component and none with the masering component L_2. A similar situation exists with the component L_2 in the $4_{-1} - 3_0E$ multiplet at 36 GHz of *E*-methanol (panel 7 in Fig. 6): there are four 'favoured' components (L_1, L_2, R_1, R_2), but only three of them (L_1, R_1, R_2) are observed as masers. It appears that the probability to form a maser is the lowest just for the high-frequency component among the 'favoured' ones.

In general, the probability of the stimulated emission, $P(i \rightarrow j)$, is proportional to the Einstein coefficient $B \sim A/f^3$, where f is

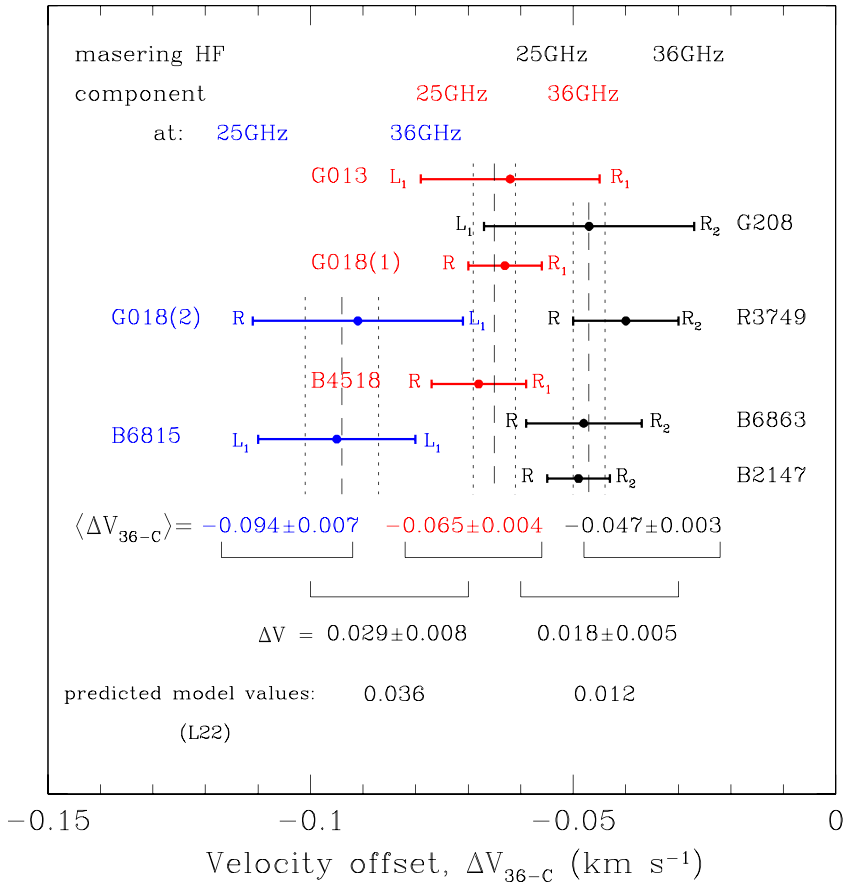

Figure 8. The peak velocities of the 36 GHz line relative to the common reference velocity V_C of the 25 GHz lines which accounts for the masering HF component at 25 GHz as they are shown in Fig. 7. Groups with matching masering HF components of the 36 GHz multiplet are marked in different colors. See text for details.

the transition frequency. Then, for a given HF transition $P(i \rightarrow j) \sim (A_{ij}/f_0^3)(1 - 3\Delta f/f_0)$, and Δf is the frequency shift between the HF transition and the multiplet centre f_0, i.e. with increasing Δf the probability decreases. However, in our case $\Delta f \sim 10$ kHz and $f_0 \sim 10$s GHz which makes the ratio $\Delta f/f_0$ extremely small. Thus, to explain the revealed absence of high-frequency masering components in the HF multiplets by the Einstein B coefficients requires a very fine tuning of the masering processes which is hard to imagine. More likely is that some pumping peculiarity is responsible for this.

In our previous study, by analysing the 44 and 95 GHz masers in *A*-methanol, we found that the masering components at these frequencies were locked, i.e. the components occurred in combinations, either R–R or L–L (L22). Now dealing with the 25 and 36 GHz masers in *E*-methanol, we do not see any component locked – all possible combinations of masering components are realized (Fig. 8), except high-energy components (L) discussed above.

In order to be formed, a maser requires first the inverted population of specific levels and then special physical conditions in the medium where the beam propagates. Whether a single masering HF component is selected by some kind of anisotropic pumping, or by some characteristics of the gain (ambient) medium, or by both factors remains at the moment completely unclear. More investigations are needed to reveal all the physical processes behind the cosmic masers.

5 CORRECTION OF THE REST FREQUENCIES FOR THE $4_{-1} - 3_0E$, $7_0 - 6_1A^+$, AND $8_0 - 7_1A^+$ METHANOL TRANSITIONS

In this study and in L22, we analysed Class I masers in the $7_0 - 6_1A^+$ at 44 GHz and $8_0 - 7_1A^+$ at 95 GHz transitions of *A*-methanol together with the $4_{-1} - 3_0E$ transition at 36 GHz and several transitions at 25 GHz of *E*-methanol observed towards the same Galactic targets. The rest frequencies (centres of multiplets) of the transitions at 25 GHz are measured in the laboratory with an accuracy higher than 1 kHz, whereas all other rest frequencies are known with larger uncertainties of ~ 10 kHz (Table 2). Class I methanol masers arise in compact (linear scale $\lesssim 100$ au) regions of a cold and quiet gas with small velocity gradients. Maser line profiles are simple, narrow, and stable. It is natural to suppose that all observed masers originate in the same velocity field and, hence, all line positions should coincide. Then the poorly known rest frequencies can be corrected via the common procedure, where lines with frequencies to be adjusted are aligned with some reference line (e.g. Dore et al. 2004; Pagani et al. 2009; Voronkov et al. 2014).

As a reference we chose the $5_2 - 5_1E$ line at 25 GHz for reasons already mentioned above: this line is strong, so its position (peak velocity) can be calculated with small errors, and its laboratory profile with a partly resolved HF structure had spacing and S/N ratio high enough to estimate the frequencies of individual HF components more or less accurately.

From the analysis performed in the previous section, we know which HF component of the 25 GHz is masering in each source. According to the calculations carried out with the laboratory profiles, the component L_1 coincides within the measurement errors ($0.006\,\mathrm{km\,s^{-1}}$) with the multiplet centre and the component R is detached from it by $0.100 \pm 0.006\,\mathrm{km\,s^{-1}}$, so that the difference between these components is $0.100 \pm 0.008\,\mathrm{km\,s^{-1}}$ (Table 4). From the observed maser profiles we measure $0.093 \pm 0.004\,\mathrm{km\,s^{-1}}$. This is a more accurate estimate, especially taking into account that in the laboratory profile the component R represents probably a close blend of two or more subcomponents, so that the position of a subcomponent which is in fact masering can be slightly shifted from the position of the blend centre. Thus, in the following calculations we consider the HF component L_1 as coinciding with the $5_2 - 5_1E$ multiplet centre and the HF component R – detached from it by $0.093 \pm 0.004\,\mathrm{km\,s^{-1}}$.

For the $7_0 - 6_1A^+$ transition at 44 GHz and $8_0 - 7_1A^+$ transition at 95 GHz we take the shifts of the masering components R and L relative to the corresponding multiplet centres as computed by the quantum-chemical model of Lankhaar et al. (2016, 2018). The correctness of these shifts was confirmed observationally both in L22 and in this study.

The situation with the $4_{-1} - 3_0E$ multiplet at 36 GHz is more ambiguous. We measure shifts of three masering components relative to each other and these shifts coincide within errors with those calculated by the model. However, we have no data to estimate whether the computed shifts of the HF components relative to the multiplet centre are also correct or not. Taking into account that in general the model described the HF structure of the $4_{-1} - 3_0E$ multiplet quite properly, we attribute for the component L_1 the shift relative to the multiplet centre as computed by the model and adjust the shifts of other components R_1 and R_2 accordingly.

The frequency correction based on the line alignment is conveniently performed on the velocity scale. Assuming the coinciding positions of all our maser lines, we can write the following equation:

$$V_{25} + \Delta V_{25}^{\mathrm{HF}} = V_{\mathrm{X}} + \Delta V_{\mathrm{X}}^{\mathrm{HF}} + \Delta V_{\mathrm{X}}^{\mathrm{cor}}\,. \tag{4}$$

Here the reference velocity, V_{25}, and the velocity of the corrected species X, V_{X}, are measured from the observed sky frequencies using radio convention and are given in Table 7. The values of $\Delta V_{25}^{\mathrm{HF}}$ and $\Delta V_{\mathrm{X}}^{\mathrm{HF}}$ are the shifts relative to the multiplet centre of the masering HF components (indicated for our targets in Figs 7 and 8), and $\Delta V_{\mathrm{X}}^{\mathrm{cor}}$ is the velocity correction for the adjusted X line.

The corresponding frequency correction, $\Delta f_X^{\mathrm{cor}}$ is then calculated as:

$$\Delta f_{\mathrm{X}}^{\mathrm{cor}} = \frac{f_{\mathrm{X}} \cdot \Delta V_{\mathrm{X}}^{\mathrm{cor}}/c}{1 - V_{\mathrm{X}}/c - \Delta V_{\mathrm{X}}^{\mathrm{cor}}/c} \approx f_{\mathrm{X}} \cdot \Delta V_{\mathrm{X}}^{\mathrm{cor}}/c\,, \tag{5}$$

taking into account that the quantities $V_{\mathrm{X}}/c \ll 1$, and $\Delta V_{\mathrm{X}}^{\mathrm{cor}}/c \ll 1$.

The calculated velocity corrections, $\Delta V_{\mathrm{X}}^{\mathrm{cor}}$, for the methanol transitions at 44 and 36 GHz are listed in Table 8. The low dispersion of the obtained values in both cases indicates that the masering HF components and their shifts were estimated properly.

The resulting means $\Delta V_{44}^{\mathrm{cor}} = -0.0842 \pm 0.0013\,\mathrm{km\,s^{-1}}$ and $\Delta V_{36}^{\mathrm{cor}} = 0.0899 \pm 0.0015\,\mathrm{km\,s^{-1}}$ give the frequency corrections $\Delta f_{44}^{\mathrm{cor}} = -0.0124 \pm 0.0002$ MHz and $\Delta f_{36}^{\mathrm{cor}} = 0.0108 \pm 0.0002$ MHz.

In L22, we calculated the velocity difference ΔV_{44-95} for 19 Galactic targets. Using the adjusted rest frequency for the transition at 44 GHz, we can now correct the rest frequency of the $8_0 - 7_1A^+$ transition at 95 GHz. The average of the velocity corrections given in Table 9 is $\Delta V_{95}^{\mathrm{cor}} = -0.0679 \pm 0.0009\,\mathrm{km\,s^{-1}}$ with corresponding correction in frequency $\Delta f_{95}^{\mathrm{cor}} = -0.0216 \pm 0.0003$ MHz.

The frequency of our reference line $5_2 - 5_1E$ is known with an error of 0.4 kHz (Table 2) which can be considered as a systematic error. Taking this into account, we obtain the following corrected frequencies: $f_{36} = (36\,169.2488 \pm 0.0002_{\mathrm{stat}} \pm 0.0004_{\mathrm{sys}})$ MHz, $f_{44} = (44\,069.4176 \pm 0.0002_{\mathrm{stat}} \pm 0.0004_{\mathrm{sys}})$ MHz, and $f_{95} = (95\,169.4414 \pm 0.0003_{\mathrm{stat}} \pm 0.0004_{\mathrm{sys}})$ MHz.

Table 8. Velocity corrections ΔV^{cor} for methanol transitions at 44 and 36 GHz calculated by equation (5). The 1σ uncertainties in the last digits are given in parentheses.

Source	$\Delta V_{44}^{\mathrm{cor}}$ ($\mathrm{km\,s^{-1}}$)	$\Delta V_{36}^{\mathrm{cor}}$ ($\mathrm{km\,s^{-1}}$)
B2147	−0.083(3)	0.092(6)
B6863	−0.080(5)	0.091(11)
R3749	−0.090(6)	0.083(10)
G018(2)	−0.090(19)	0.087(20)
G018(1)	−0.094(9)	0.088(9)
G013	−0.091(12)	0.087(19)
R2879	−0.083(4)	–
G208	−0.097(18)	0.090(20)
B6815	−0.083(9)	0.091(15)
B4518	–	0.093(9)
Weighted mean:	−0.0842(13)	0.0899(11)

Table 9. Velocity correction for the difference $\left(V_{44}^{\mathrm{P}} - V_{95}^{\mathrm{M}}\right)$ measured in L22 for methanol transitions at 44 and 95 GHz. The 1σ uncertainties in the last digits are given in parentheses.

Source	$\Delta V_{44}^{\mathrm{P}} - V_{95}^{\mathrm{M}}$ ($\mathrm{km\,s^{-1}}$)		$\Delta V_{44}^{\mathrm{cor}} - V_{95}^{\mathrm{M}}$ ($\mathrm{km\,s^{-1}}$)
R149	0.005(12)	L	−0.072(12)
R153	0.024(25)	R	−0.08(3)
R2837	0.031(40)	R	−0.07(4)
R2879	0.036(5)	R	−0.064(5)
R3659	0.013(15)	L	−0.064(15)
R3749	0.029(8)	R	−0.071(8)
R3865	0.033(8)	R	−0.067(8)
B4252	0.008(4)	L	−0.069(4)
B1584	0.008(30)	L	−0.07(3)
B7501	0.035(11)	R	−0.065(11)
B7022	0.025(8)	R	−0.075(8)
B2147	0.046(20)	R	−0.05(2)
B4518	0.014(18)	L	−0.063(18)
B6518	0.030(8)	R	−0.070(8)
B6820(1)	0.032(19)	R	−0.068(19)
B6820(2)	0.034(30)	R	−0.07(3)
B6863	0.024(20)	R	−0.06(2)
G029	0.009(9)	L	−0.068(9)
G018	0.016(19)	L	−0.061(19)
	Weighted mean:		−0.0679(9)

6 CONCLUSIONS AND FUTURE PROSPECTS

With the Effelsberg 100-m radio telescope, we carried out simultaneous observations of Class I methanol masers at frequencies 25, 36, and 44 GHz towards 22 Galactic targets located at Galactocentric distances from 5 to 13 kpc. Comparison with previous observations of the 44 GHz masers performed 6–10 yr earlier with the KVN towards the same targets confirmed the kinematic stability of the Class I maser

line profiles and revealed a systematic shift of 0.013 ± 0.005 km s^{-1} in radial velocities between the two telescopes.

Lankhaar et al. (2016, 2018) developed from first principles a quantum-chemical model for the hyperfine structure in methanol and computed frequency shifts of individual HF components relative to the centres of various torsion–rotational multiplets. Among others, they assumed that in every multiplet there are only a few specific ('favoured') HF transitions (with largest Einstein A coefficients) which predominantly form masers.

In our previous study (L22), by analysing Class I masers at 44 and 95 GHz in *A*-methanol observed towards 19 Galactic targets, we confirmed the model predictions that each of the $7_0 - 6_1A^+$ (44 GHz) and $8_0 - 7_1A^+$ (95 GHz) transitions has two 'favoured' HF components – one to the left and one to the right of the multiplet centre – and found that only one of them is masering in any given source.

The present observations were carried out with the aim to test whether the assumption of the hyperfine-specific effects in the maser action is valid also for other Class I masers, in particular for transitions at 25 and 36 GHz in *E*-methanol, and to identify the masering components in the corresponding HF multiplets.

The obtained main results are as follows:

(i) We reprocessed the laboratory spectra of several transitions in the *E*-type ground torsional state ($v_t = 0$) of CH_3OH recorded in 2012 with the microwave molecular beam spectrometer of the Hannover University. The S/N ratio in the obtained line profiles made it possible to deconvolve the hyperfine structure of the multiplets, in particular that of the $5_2 - 5_1E$ (24 959 MHz) transition which is usually observed as a strong Class I maser. 'Favoured' HF components were identified.

(ii) Among the observed 22 targets selected from methanol maser catalogues compiled on base of the 44 GHz observations, only nine targets (10 maser sources) showed the simultaneous activity of masers at 25, 36, and 44 GHz. A detailed analysis of all observed maser line profiles was carried out and the line peak (radial) velocities were determined. With these velocities, the differences ΔV_{36-25} and ΔV_{44-25} were calculated. At 25 GHz, the maser line widths are much narrower than the splitting between the 'favoured' HF components, which confirms the result previously obtained for the 44 and 95 GHz masers: namely, that only one HF component is acting in any one maser source.

(iii) As expected, the calculated values ΔV_{44-25} form separate groups. With masering HF components at 44 GHz known from the previous study and using the HF component structure obtained from the laboratory spectrum of the $5_2 - 5_1E$ multiplet as a template, we compared the differences between the groups with the splitting between the 'favoured' components in the template and determined for every source which particular HF component acted as the 25 GHz maser. The $5_2 - 5_1E$ multiplet has three 'favoured' components. Among 10 sources we detected six masers formed by the low-frequency component, four by the middle-frequency component, and none with the high-frequency component.

(iv) The velocity differences ΔV_{36-25} form separate groups as well. The template of the HF structure at 36 GHz was computed with the quantum-chemical model by Lankhaar et al. (2016, 2018). Using the same procedure, i.e. comparing the differences between the groups with the splitting between the 'favoured' components in the template, we identified the masering components in the 36 GHz masers. The model predicts four 'favoured' components, but we observed as masers only three of them. Again no masers with the high-frequency component were found.

(v) The laboratory rest frequencies of the $4_{-1} - 3_0E$ (36 GHz), $7_0 - 6_1A^+$ (44 GHz), and $8_0 - 7_1A^+$ (95 GHz) multiplet centres were known with accuracies of about 10 kHz, whereas the rest frequency of the $5_2 - 5_1E$ (25 GHz) transition was measured with an order of magnitude higher accuracy. Using the common procedure of the line alignment and accounting for a particular HF component which forms a maser in a specific source, we corrected the rest frequencies of these transitions. The refined rest frequency values are as follows: $f_{36} = (36\,169.2488 \pm 0.0002_{stat} \pm 0.0004_{sys})$ MHz, $f_{44} = (44\,069.4176 \pm 0.0002_{stat} \pm 0.0004_{sys})$ MHz, and $f_{95} = (95\,169.4414 \pm 0.0003_{stat} \pm 0.0004_{sys})$ MHz.

The present analysis is based entirely on the kinematic characteristics of the maser line profiles. For all masers both in *A*- and *E*-methanol, we confirm that they are formed by only one HF component and this component varies from source to source. Among components indicated as 'favoured', we do not observe in the *E*-methanol masers at 25 and 36 GHz the high-frequency HF component acting. In general, it is quite obvious, that both the pumping of the inverted population and the formation of the maser radiation itself should be in some way modulated by physical and chemical conditions in the gain medium. It is also clear that this modulation should be fine-tuned, taking into account very small frequency differences between particular HF components. However, at the moment the mechanism behind the anisotropic pumping of methanol masers remains completely obscure. It is to note that anomalous effects related to the HF structures in different molecules are well known, but in spite of many studies (e.g. Field 1985; Park 2001; Camarata et al. 2015; Zhou et al. 2020; Lankhaar et al. 2018, 2024) the problems are still far from being solved.

ACKNOWLEDGEMENTS

We are grateful to the staff of the Effelsberg 100-m telescope observatory for assistance in our observations. We also thank J.-U. Grabow for laboratory measurements of methanol lines at the Hannover University. SAL was supported in part by the Russian Science Foundation under grant no. 23-22-00124. OSB acknowledges financial support from the Italian Ministry of University and Research – Project Proposal CIR01-00010.

DATA AVAILABILITY

The data underlying this article will be shared on reasonable request to the corresponding author.

REFERENCES

Argon A. L., Reid M. J., Menten K. M., 2000, ApJS, 129, 159
Bae J.-H., Kim K.-T., Youn S.-Y., Kim W.-J., Byun D.-Y., Kang H., Oh C. S., 2011, ApJS, 196, 18
Barrett A. H., Schwartz P. R., Waters J. W., 1971, ApJ, 168, L101
Batrla W., Matthews h. E., Menten K. M., Walmsley C. M., 1987, Nature, 326, 49
Bayandina O. S., Burns R. A., Kurtz S. E., Shakhvorostova N. N., Val'tts I. E., 2019, ApJ, 884, 140
Belov S. P. et al., 2016, J. Chem. Phys., 145, 024307
Breen S. L., Contreras Y., Dawson J. R., Ellingsen S. P., Voronkov M. A., McCarthy T. P., 2019, MNRAS, 484, 5072
Camarata M. A., Jackson J. M., Chambers E., 2015, ApJ, 806, 74
Coudert L. H., Guttlé C., Huet T. R., Grabow J.-U., Levshakov S. A., 2015, J. Chem. Phys., 143, 044304
Cragg D. M., Sobolev A. M., Goddfrey P. D., 2005, MNRAS, 360, 533

Crutcher R. M., Kemball A. J., 2019, Front. Astron. Space Sci., 6, 66
Cyganowski C. J., Brogan C. L., Hunter T. R., Churchwell E., 2009, ApJ, 702, 1615
Daprà M. et al., 2017, MNRAS, 472, 4434
Dore L. et al., 2004, A&A, 413, 1177
Field D., 1985, MNRAS, 217, 1
Fontani F., Cesaroni R., Furuya R. S., 2010, A&A, 517, A56
Gaia Collaboration et al., 2018, A&A, 616, A1
Grabow J.-U., 2004, Chemische Bindung und interne Dynamik in großen isolierten Molekülen: Rotationsspektroskopische Untersuchung. Dem Fachbereich Chemie der Universität, Hannover
Grabow J.-U., 2011, in Quack M., Merkt F., eds, Handbook of High-Resolution Spectroscopy. John Wiley & Sons, Chichester, p. 723
Green J. A. et al., 2017, MNRAS, 469, 1383
Haschick A. D., Menten K. M., Baan W. A., 1990, ApJ, 354, 556
Heuvel J., Dymanus A., 1973a, J. Mol. Spectrosc., 45, 282
Heuvel J., Dymanus A., 1973b, J. Mol. Spectrosc., 47, 363
Hougen J., Kleiner I., Godefroid M., 1994, J. Mol. Spectrosc., 163, 559
Jansen P., Xu L.-H., Kleiner I., Ubachs W., Bethlem H. L., 2011, Phys. Rev. Lett., 106, 100801
Kalenskii S. V. et al., 2010, MNRAS, 405, 613
Kalenskii S. V., Bachiller R., Berulis I. I., Valtts I. E., Gomez-Gonzalez J., Martin-Pintado J., Rodriguez-Franco A., Slysh V. I., 1992, Soviet Astronomy, 36, 517
Kalenskii S. V., Slysh V. I., Val'tts I. E., Dzura A. M., 1996, Int. Astron. Union Symp., 170, 49
Kalenskij S. V. et al., 1992, Proceed. Conf. Astrophysical Masers. Springer-Verlag, Berlin, p. 191
Kang J., Byun D.-Y., Kim K.-T., Kim J., Lyo A.-R., Vlemmings W. H. T., 2016, ApJS, 227, 18
Kim C.-H., Kim K.-T., Park Y.-S., 2018, ApJS, 236, 31
Kim W.-J., Kim K.-T., Kim K.-T., 2019, ApJS, 244, 33
Klein B., Hochgürtel S., Krämer I., Bell A., Meyer K., Güsten R., 2012, A&A, 542, L3
Kurtz S., Hofner P., Alvarez C. V., 2004, ApJS, 155, 149
Ladeyschikov D. A., Bayandina O. S., Sobolev A. M., 2019, AJ, 158, 233
Ladeyschikov D. A., Urquhart J. S., Sobolev A. M., Breen S. L., Bayandina O. S., 2020, AJ, 160, 213
Lankhaar B., Groenenboom G. C., van der Avoird A., 2016, J. Chem. Phys., 145, 244301
Lankhaar B., Surcis G., Vlemmings W., Impellizzeri V., 2024, A&A, 683, 117
Lankhaar B., Vlemmings W., Surcis G., van Langenvelde H. J., Groenenboom G. C., van der Avoird A., 2018, Nat. Astron., 2, 145L
Leurini S., Menten K. M., Walmsley C. M., 2016, A&A, 592, A31
Levshakov S. A. et al., 2019, MNRAS, 487, 5175
Levshakov S. A. et al., 2022, MNRAS, 511, 413 (L22)
Levshakov S. A., Kozlov M. G., Reimers D., 2011, ApJ, 738, 26
Liechti S., Wilson T. L., 1996, A&A, 314, 615
Mehrotra S. C., Dreizler H., MÃd'der H., 1985, Z. Nat.forsch., 40a, 683
Menten K. M., 1991, in Haschick A. D., Ho P. T. P., eds, Proc. Third Haystack Observatory Meeting. Astron. Soc. Pac., San Francisco, p. 119
Menten K. M., Reid M. J., Pratar P., Moran J. M., Wilson T. L., 1992, ApJ, 401, L39
Menten K. M., Walmsley C. M., Henkel C., Wilson T. L., 1986, A&A, 157, 318
Menten K. M., Walmsley C. M., Henkel C., Wilson T. L., 1988, A&A, 198, 267
Minier V., Conway J. E., Booth R. S., 2001, A&A, 369, 278
Momjian E., Sarma A. P., 2019, ApJ, 872, 12
Müller H. S. P., Menten K. M., Mäder H., 2004, A&A, 428, 1019
Pagani L. et al., 2017, A&A, 604, 32
Pagani L., Daniel F., Dubernet M.-L., 2009, A&A, 494, 719
Park Y.-S., 2001, A&A, 376, 348
Pickett H. M., Poynter R. L., Cohen E. A., Delitsky M. L., Pearson J. C., Müller H. S. P., 1998, J. Quant. Spectrosc. Radiat. Transfer, 60, 883
Plambeck R. L., Menten K. M., 1990, ApJ, 364, 555
Sarma A. P., Momjian E., 2009, ApJ, 705, L176
Sarma A. P., Momjian E., 2020, ApJ, 890, 6
Sobolev A. M., Deguchi S., 1994, A&A, 291, 569
Tsunekawa S., Ukai T., Toyama A., Takagi K., 1995, Toyama Microwave Atlas for Spectroscopists and Astronomers. Department of Physics, Toyama University, Japan, Available at:https://www.sci.u-toyama.ac.jp/phys/4ken/atlas/
van Terwisga S. E., Hacar A., van Dishoeck E. F., 2019, A&A, 628, A85
Vlemmings W. H. T., 2008, A&A, 484, 773
Voronkov M. A., Caswell J. L., Ellingsen S. P., Green J. A., Breen S. L., 2014, MNRAS, 439, 2584
Vorotyntseva J. S., Kozlov M. G., Levshakov S. A., 2024, MNRAS, 527, 2750
Vorotyntseva J. S., Levshakov S. A., 2024, Astron. Astrophys. Trans., 34, in press,
Wenner N., Sarma A. P., Momjian P., 2022, ApJ, 930, 114
Xu L.-H. et al., 2008, J. Mol. Spectrosc., 251, 305
Yang W. et al., 2020, ApJS, 248, 18
Zhou D.-D. et al., 2020, A&A, 640, 114

This paper has been typeset from a TEX/LATEX file prepared by the author.